UC Berkeley
UC Berkeley Previously Published Works

Title

A New Strategy for High-Voltage Cathodes for K-Ion Batteries: Stoichiometric KVPO4F

Permalink

Journal

ISSN

Authors

Kim, Haegyeom
Seo, Dong-Hwa
Bianchini, Matteo
et al.

Publication Date

DOI

Peer reviewed

A new strategy for high voltage cathodes for K-ion batteries: stoichiometric KVPO$_4$F

Haegyeom Kim, Dong-Hwa Seo, Matteo Bianchini, Raphaële J. Clément, Hyunchul Kim, Jae Chul Kim, Won-Sub Yoon, Gerbrand Ceder[*]

Dr. H. Kim, Dr. M. Bianchini, Dr. H. Kim, Dr. J. C. Kim
Materials Sciences Division, Lawrence Berkeley National Laboratory, Berkeley, CA 94720, USA
Dr. D. –H. Seo, Dr. R. J. Clément
Department of Materials Science and Engineering, University of California, Berkeley, CA 94720, USA
Prof. W. –S. Yoon
Department of Energy Science, Sungkyunkwan University, Suwon, 16419, Republic of Korea
Prof. G. Ceder
Materials Sciences Division, Lawrence Berkeley National Laboratory, Berkeley, CA 94720, USA
Department of Materials Science and Engineering, University of California, Berkeley, CA 94720, USA
E-mail: gceder@berkeley.edu

Abstract

The exploration of high-energy-density cathode materials is vital to the practical use of K-ion batteries. Layered K-metal oxides have too high voltage slope to be practical due to their large K$^+$-K$^+$ interaction, making 3D polyanion materials more relevant. Here, we develop stoichiometric KVPO$_4$F for use as a high-energy-density K-ion cathode. The KVPO$_4$F cathode delivers a reversible capacity of ~105 mAh g^{-1} with an average voltage of ~4.3 V (vs. K/K$^+$), resulting in a gravimetric energy density of ~450 Wh kg^{-1}. During electrochemical cycling, the K$_x$VPO$_4$F cathode goes through various intermediate phases at x = 0.75, 0.625, and 0.5 upon K extraction and reinsertion, as determined by ex situ X-ray diffraction characterization and *ab-initio* calculations. This work further explains the role of oxygen substitution in KVPO$_{4+x}$F$_{1-x}$: the oxygenation of KVPO$_4$F leads to an anion-disordered

structure which prevents the formation of K^+/vacancy orderings without electrochemical plateaus and hence to a smoother voltage profile.

1. Introduction

Li-ion batteries (LIBs) dominate the global market for portable and automotive energy storage technologies because of their high energy density. Their use is even expanding to large-scale applications such as grid-level energy storage systems. However, the question of whether Li reserves[1] or the metal required for the cathode compounds[2] can meet the demand for large-scale applications remains under debate. In response, Na-ion batteries (NIBs) and K-ion batteries (KIBs) have been studied as alternative energy storage technologies systems because of the global abundance of Na and K.[3-7] When compared to NIBs, KIBs are particularly interesting because (i) K/K^+ has a lower standard redox potential than Na/Na^+, which can be translated into a higher working voltage,[5] and (ii) graphite can intercalate K ions, forming a stable KC_8 compound, whereas no stable NaC_x compounds are present in the Na–graphite system.[5, 8-12]

Layered transition metal oxides (TMOs) have been considered promising candidates for LIB and NIB cathodes because of their dense close-packed structure as well as their high Li and Na diffusivities.[13-15] In this respect, K-TMOs, including K_xCoO_2 (x= 0.41, 0.6, and 0.67),[16-17] K_xMnO_2 (*x*= 0.3 and 0.5),[18-19] $K_{0.7}Fe_{0.5}Mn_{0.5}O_2$,[20] and $K_{0.67}Ni_{0.17}Co_{0.17}Mn_{0.66}O_2$,[21] have been investigated as cathode materials for KIBs. However, the specific capacities and working voltage of K-TMOs are lower than those of Li- and Na-TMOs due the strong K^+-K^+ interaction which is much larger than the corresponding Li^+–Li^+ or Na^+–Na^+ interactions.[16-21] The strong K^+-K^+ interaction is due to the large size of K^+ which increases the distance between the oxygen layers and reduces their effectiveness in screening the K^+-K^+ electrostatic repulsion. This strong interaction results in greater voltage slope and low specific capacity between set voltage limits for layered K-TMOs.

Polyanionic compounds may be better cathode candidates because they exist in various structural frameworks in which the K ions are three-dimensionally arranged and separated by large polyanions, effectively reducing the strength of the K^+–K^+ repulsion. The weaker K^+–K^+ interaction can lead to a higher working voltage, as demonstrated in some polyanionic compounds such as $K_3V_2(PO_4)_3$,[22] $FeSO_4F$,[23] and KVP_2O_7 [24]. Nevertheless, the achieved energy density of K-polyanionic compounds remains far below those of current LIB and NIB cathodes. Therefore, it is vital to explore new cathode materials for the development of high-energy-density KIBs.

Fluorophosphates, including $AVPO_4F$ (A = Li and Na)[25-28] and Li_2MPO_4F (M = Fe and Mn)[29-30], continue to attract considerable attention as cathode materials for LIBs and NIBs because of their high working voltage. Recently, Fedotov *et al.* reported $LiVPO_4F$ prepared by Li/K ion-exchange from $KVPO_4F$ with a $KTiOPO_4$-type structure. This Li-ion cathode delivers operates at ~4.0 V (*vs.* Li/Li^+) with a specific capacity of ~110 mAh g^{-1}.[31] This recent discovery motivates our investigation of the structural and electrochemical properties of $KVPO_4F$ for use as a KIB cathode. Specifically, in this work, we investigate the structure of as-synthesized $KVPO_4F$ using ^{31}P solid-state nuclear magnetic resonance (NMR) spectroscopy and X-ray diffraction (XRD), and the structural evolution of the material during K de/intercalation using *ex situ* XRD and ab-initio calculations. Our findings demonstrate the consecutive occurrence of several two-phase reactions in the material upon K de/intercalation. We further explain how the fluorine:oxygen ratio in $KVPO_{4+x}F_{1-x}$ affects its electrochemistry. The oxygenation of $KVPO_4F$ results in a more disordered structure, leading to a smoother voltage profile. However, the oxygenation of $KVPO_4F$ increases the initial V valence state and thus reduces the achievable specific capacity because of the more limited V redox availability. Oxygen substitution for fluorine also lowers the operating voltage because of the reduced inductive effect resulting from the lower fluorine concentration in the material.[32]

2. Results

2.1. **Material characterization of KVPO₄F**

Figure 1a presents a synchrotron-based XRD pattern of $KVPO_4F$ powder and its Rietveld refinement result using the $Pna2_1$ space group. The crystal structure of $KVPO_4F$ is isostructural with orthorhombic $KTiOPO_4$. However, the structures differ in the connectivity between the transition metal octahedra: TiO_6 units are connected to one another *via* O in $KTiOPO_4$, whereas VO_4F_2 units are connected *via* F in $KVPO_4F$. Refinement of the synchrotron XRD data (Table 1 in Supplementary Information) yields lattice parameters of a = 12.8423(1) Å, b = 6.40785(3) Å, and c = 10.62974(6) Å. In the refinement, the calculated bond valence sum of the two vanadium sites is +2.98(2) and +2.97(2), suggesting the presence of V^{3+} in the compound. Elemental analysis using inductively coupled plasma for K, V, P, and the ion selective electrode (ISE) method for F also indicates a K:V:P:F ratio of 1.04:1.00:0.96:0.96, which suggests that the composition of our $KVPO_4F$ material is very close to the stoichiometric composition. Figures 1b and 1c present the crystal structure of $KVPO_4F$ projected along the b- and a-axis, respectively. In the structure, VO_4F_2 octahedra are interconnected *via* corner-sharing PO_4 tetrahedra along the a and b axes. The F atom can occupy equatorial or axial positions around the V atom (V1 and V2 sites, respectively), and the VO_4F_2 octahedra share one F atom at the corner, forming zig-zag chains, which are then bridged *via* PO_4 tetrahedra as observed in Figure 1d. In the local vanadium environments, VO_4F_2 octahedra are surrounded by four PO_4 tetrahedra and two VO_4F_2 octahedra, as illustrated in Figure 1e. The V1 site is equatorially surrounded by four PO_4 tetrahedra and two VO_4F_2 octahedra (V2 site) at axial direction. In contrast, The V2 site is surrounded by three PO_4 tetrahedra and one VO_4F_2 octahedron (V1 site) in the equatorial plane and one PO_4 tetrahedron and VO_4F_2 octahedron (V1 site) in the axial direction. In the crystal structure of $KVPO_4F$, K ions occupy two 9-coordinate KO_7F_2 environments located at K1 and K2 sites with a three-dimensional arrangement, as shown in Figure 1b–c. The K1 site shares F with

4

two VO_4F_2 octahedra (Figure 1f), whereas the K2 site shares a F–F edge with one VO_4F_2 octahedron (Figure 1g). One should note that we compared our results of Rietveld refinements obtained using the structural models reported by Chihara *et al.*[33] and Fedotove *et al.*[31] and found a better agreement with the latter. In our refinement, K1 and K2 are both split between two sites, which are very close to each other, and thus, each has an occupancy factor of 0.5. The particle size of $KVPO_4F$ is estimated from scanning electron microscopy analysis to be in the range of 20–200 nm (see Supplementary Figure 1). Thermogravimetric analysis reveals that the $KVPO_4F$ material contains ~3.3% carbon by weight, as shown in Supplementary Figure 2.

2.2. **Electrochemical K-storage properties of KVPO₄F**

Figure 2a shows the voltage *vs.* capacity curves of $KVPO_4F$ for the first two charge/discharge cycles between 3–5 V and a current rate of 5 mA g^{-1}. The first charge and discharge capacities are ~140 and ~105 mAh g^{-1}, respectively. Each charge and discharge voltage profile exhibits four distinct plateaus, indicating successive phase transitions as the K content changes. The identical voltage shape between charge and discharge curves demonstrates that K extraction and re-insertion processes are reversible. In turn, the differential capacity (dQ dV^{-1}) curve in Figure 2b clearly displays four oxidation peaks at 4.04 (O1), 4.24 (O2), 4.41 (O3), and 4.87 (O4) V during charge and four reduction peaks at 3.97 (R1), 4.21 (R2), 4.34 (R3), and 4.72 V (R4) during discharge, demonstrating multiple reversible phase transitions upon cycling. Figure 2c shows the rate capability of $KVPO_4F$ at current rates of 5, 10, 30, 50, 80, 100, 150, and 300 mA g^{-1}. $KVPO_4F$ delivers a specific capacity of 102, 101, 92, 82, 72, 65, 56, and 44 mAh g^{-1} at the respective rates. The capacity and coulombic efficiency of $KVPO_4F$ as a function of cycle number at 5 mA g^{-1} are plotted in Figure 2d. $KVPO_4F$ maintains a reversible capacity of 78 mAh g^{-1} (75% retention compared with that of the 1st discharge) after 30 cycles. The coulombic efficiency is low (~95%), leading to poor capacity retention. The low coulombic efficiency indicates that the anodic current is larger than the

cathodic current, which can result from decomposition of cathode materials and/or electrolyte degradation upon charging at high voltage (> 4.5 V). To rationalize the origin of capacity fading, we investigate the structural stability of KVPO$_4$F upon cycling using *ex situ* XRD and verify the health of the electrolyte upon charging using linear scan voltammetry. No noticeable structural change is observed in the *ex situ* XRD patterns of the KVPO$_4$F cathode after 30 cycles, as shown in Supplementary Figure 3. However, the linear scan voltage measurement of the K-electrolyte in Supplementary Figure 4 indicates that the anodic current starts to gradually increase at ~4 V and abruptly increases near 5.0 V (*vs.* K/K$^+$). Hence, the K-electrolyte is unstable at high voltage, which may be the origin of the low coulombic efficiency. It is likely that this leads to decomposition products on the cathode surface which increase impedance and thereby decrease effective capacity.

A plot of the average voltage *vs.* reversible capacity of various K-ion cathode materials as well as selected NIB and LIB cathodes is presented in **Figure 3**.[16, 19-20, 22-24, 26, 33-38] Our KVPO$_4$F electrode provides a high average discharge voltage of 4.33 V, which is the highest value among KIB cathode materials reported to date.[16, 19-22, 24, 33-34] Notably, the average voltage of KVPO$_4$F reported here is ~0.2-V higher than that reported by Chihara *et al.* for a similar compound.[33] This discrepancy is likely attributable to the different local structures and compositions of the two compounds, which will be discussed in more detail in the discussion section of this paper. Moreover, the voltage of KVPO$_4$F is also higher than that of other vanadium-containing polyanionic compounds for Li and Na systems such as NaVPO$_4$F, Na$_3$V$_2$(PO$_4$)$_2$F$_3$, Na$_7$V$_2$(PO$_4$)$_2$F$_3$, and LiVPO$_4$F.[25, 35-38]

2.3. **Structural evolution during charge and discharge of KVPO$_4$F**

Figure 4a presents the formation energies of K$_x$VPO$_4$F (x = 1, 0.875, 0.75, 0.625, 0.5, 0.375, 0.25, 0.125, 0) phases obtained from first-principles DFT calculations. All symmetrically distinct K$^+$/vacancy orderings within the unit cell of K$_x$VPO$_4$F including 8 formula units were generated using the enumeration technique reported by Hart *et al.*[39], and the 50

6

configurations with the lowest electrostatic energy at each K content ($0 \leq x \leq 1$) were calculated using GGA+U. For the calculations, we used the crystal structure of $KVPO_4F$ with two K (K1 and K2), both of which are split between two possible positions. These two positions are too close together to be occupied simultaneously, and thus, have partial occupancy. We find stable K^+/vacancy orderings at $x = 0.75$ and 0.5 in K_xVPO_4F. At $x = 0.625$, the lowest energy configuration is ~ 6 meV per formula unit above the convex hull with respect to decomposition into $K_{0.75}VPO_4F$ and $K_{0.5}VPO_4F$. Such a small energy difference makes it possible that $K_{0.625}VPO_4F$ is stabilized at room temperature by entropy. Overall, first-principles DFT calculations predict at least three two-phase reactions upon K extraction over the range of K contents: $1 > x > 0.75$, $0.75 > x > 0.5$, and $0.5 > x > 0$. Figure 4b compares the calculated voltage to the experimental voltage curve obtained at a current rate of 5 mA g^{-1}. We note that the calculated voltage is shifted upwards by 0.35 V for better agreement with the experimental voltage curve. The calculated voltage plot shows phase transitions at $x = 0.75$ and 0.5 in K_xVPO_4F, which is consistent with our experimental observations of voltage steps at $x = 0.75$ and 0.5. The experimentally obtained voltage curve has an additional voltage step at $x = 0.625$, which suggests the formation of a stable intermediate phase, which may be the phase that is predicted to be close to the hull in the calculations (see Figure 4a).

To better understand the structural evolution of K_xVPO_4F upon cycling, *ex situ* XRD data are collected from samples at different states of charge and discharge. **Figure 5**a presents a representative charge/discharge profile, with the points indicating the states at which the *ex situ* XRD patterns in Figure 5b–d are obtained. The K concentration is estimated by normalizing the experimentally determined specific capacity to the theoretical value. When the K content, x, decreases from 1 to 0.86, the XRD peaks at 16.6º, 26.9º, 29.3º, and 33.1º, which belong to $KVPO_4F$, slightly shift to higher angle and no additional peak evolution is observed. This indicates that K extraction occurs through a solid-solution reaction in

K_xVPO_4F when x is between 1 and 0.86. A new set of XRD peaks start to appear at 16.8º, 29.4º and 33.4º at the expense of the peak at 26.3º and 29.3º when $x = 0.79$. This new diffraction peaks are fully formed in the diffraction patterns for $x = 0.72$, which is indicative of the new ordered phase being formed around $x\sim0.72$. This is consistent with the voltage step at $x = 0.75$ in both the experimental and calculated curves in Figure 4b. In the range of $0.72 > x > 0.63$, another set of peaks appears at 16.9º, 29.5º, and 33.7º, indicating the formation of the second new phase. This result agrees well with the formation of a compound at $x\sim0.625$ in K_xVPO_4F, as discussed earlier. Further K extraction to $x\sim0.5$ generates new XRD peaks at 17.1º, 29.7º, 33.1º, and 44.0º, which indicates an additional phase transition from $K_{0.625}VPO_4F$ to $K_{0.5}VPO_4F$, consistent with the voltage step at $x\sim0.5$ in K_xVPO_4F in both the experimental and DFT calculations (Figure 4b). As the K content further decreases from $x\sim0.5$ to $x\sim0.0$, the VPO_4F phase is formed with XRD peaks at 17.2º, 29.8º, 33.5º, and 34.2º in Figure 5b–d. After discharge, the XRD pattern of the pristine $KVPO_4F$ phase is fully recovered, which indicates that the structural changes occurring upon cycling are reversible.

Supplementary Figure 5 presents the predicted structures of K_xVPO_4F for $x = 1, 0.75, 0.625, 0.5$, and 0, which reveal that K ions in K1 sites that share F with two different VO_4F_2 octahedra (see Figure 1f) are extracted first until the K content reaches $x = 0.5$. Potassium ions in K2 sites that share an F–F edge with one VO_4F_2 octahedron (see Figure 1g) are removed later. DFT calculations shows that the extraction of K ions from the K2 sites leads to a slight distortion of the PO_4 tetrahedra due to the shrinking ionic radius of V upon oxidation. Supplementary Figure 6 presents the simulated XRD patterns of K_xVPO_4F ($x = 1, 0.75, 0.625, 0.5$, and 0) based on the lowest energy structures obtained from first-principles DFT calculations. When the K concentration (x) decreases from 1 to 0.75, new XRD peaks appear near 16.2º and 32.2º at the expense of the peak at ~25.2º in the simulated XRD patterns. At the $K_{0.625}VPO_4F$ composition, XRD peaks appear at 16.15º, 28.5º, and 32.65º. Further K extraction to $x\sim0.5$ generates a new set of XRD peaks near 16.3º, 28.6º, and 32.9º. The

simulated XRD pattern of VPO$_4$F exhibits new peaks at 16.6°, 28.8°, 32.8°, and 33.5°. Overall, the evolution of the simulated XRD patterns with K content is similar to that of the *ex situ* XRD data (see Figure 5) and confirms the experimentally observed sequence of phase transitions as K is extracted/re-inserted from K$_x$VPO$_4$F, with stable intermediate phases forming at $x = 0.75$, 0.625, and 0.5. We note that the predicted peak positions differ slightly from the experimentally determined positions as DFT using GGA+U slightly over-predicts the lattice parameters.[19, 40-42] We further performed a full-pattern-matching procedure to compare the experimentally obtained *ex situ* XRD patterns with the simulated XRD patterns at specific K concentrations. Supplementary Table 2 lists the refined lattice parameters of K$_x$VPO$_4$F at $x = 1.0$, 0.75, 0.625, 0.5, and 0 using the computed structural model. The results demonstrate that the volume of KVPO$_4$F shrinks by ~6.54% upon full K extraction, which is most likely attributable to the shrinkage of the V octahedra as V^{3+} is oxidized to V^{4+} as well as to the removal of large K ions. Notably, the magnitude of the volume change observed here upon K extraction is similar to that observed upon Li removal from LiFePO$_4$ (~6.8%).[43]

2.4. **Effect of oxygenation in KVPO$_4$F**

Fluorophosphates have been extensively studied as cathode materials for LIBs and NIBs because of their high operating voltage and, thus, high energy density.[26-30, 37] In fluorophosphates, F$^-$ can often be substituted with some O^{2-} (oxygenation), in which case charge compensation is achieved by changing the oxidation state of nearby transition metals. In these compounds, the fluorine:oxygen ratio generally plays an important role in determining the electrochemical properties, including the working voltage and reversible capacity.[44-45] For example, in tavorite LiVPO$_{4+x}$F$_{1-x}$ compounds, the average voltage and reversible specific capacity at practical current rates decrease as the fluorine content decreases. Moreover, the voltage plateaus that appear in pure oxyphosphate LiVPO$_4$O become less pronounced with mixed fluorine-oxygen compositions.[44-45] To better understand the role of the fluorine:oxygen ratio in KVPO$_4$F, we prepared an oxygen-substituted composition,

$KVPO_{4+x}F_{1-x}$, in a mildly reducing environment (see Methods section). Supplementary Figure 7 presents the synchrotron-based XRD analysis of the oxygen-substituted phase. The refinement of the synchrotron XRD data (Table 3 in Supplementary Information) gives lattice parameters of a = 12.8235 (1) Å, b = 6.39630 (6) Å, and c = 10.5860 (1) Å, which are in a good agreement with the values in the literature[31, 33] but slightly smaller than the values obtained for our stoichiometric $KVPO_4F$ sample, as shown in Figure 1a and Supplementary Table 1. The smaller lattice parameters are consistent with oxidation of V to compensate for the increased nominal negative charge due to the O^{2-} substituting for F^-. The bond valence sum results indicate that the oxidation states of the two V sites are +3.24(1) and +3.04(9) in $KVPO_{4+x}F_{1-x}$, which suggests partial oxidation of V during synthesis upon oxygenation. Elemental analysis using inductively coupled plasma for K, V, P, and the ISE method for F indicates a K:V:P:F ratio of 1:1:1:0.64 in $KVPO_{4+x}F_{1-x}$. Based on the elemental analysis, the composition of the oxygen-substituted sample is estimated to be $KVPO_{4.36}F_{0.64}$. **Figures 6**a–b present the XANES spectra of $KVPO_4F$ and $KVPO_{4.36}F_{0.64}$ with reference spectra containing V^{3+}, V^{4+}, V^{5+}, and V metal. The inset of Figure 6a presents the V K-edge XANES spectra, where the normalized intensity is 0.5 (near the inflection point); the pre-edge region of the spectra is shown in Figure 6b. The photon energies of $KVPO_4F$ at the inflection point and the pre-edge position are similar to those observed for $Li_3V_2(PO_4)_3$ only containing V^{3+}. Therefore, the oxidation state of V in $KVPO_4F$ is trivalent. In contrast, the photon energies of $KVPO_{4.36}F_{0.64}$ at its inflection point and pre-edge position lie between those of $Li_3V_2(PO_4)_3$ (V^{3+}) and V_2O_4 (V^{4+}), indicating partial oxidation of V, which is in a good agreement with the XRD refinement results.

Figure 6c presents the ^{31}P solid-state NMR double-adiabatic spin-echo spectra collected for $KVPO_4F$ and $KVPO_{4.36}F_{0.64}$. Both materials are paramagnetic, and the major source of the ^{31}P chemical shift is the hyperfine (paramagnetic) interactions between unpaired d electrons from

V^{3+} (d^2) and V^{4+} (d^1) and the P nucleus through space and *via* V–O–P and V–F–P bond pathways. There are two forms of paramagnetic interactions: isotropic Fermi contact interactions and anisotropic electron–nuclear dipolar coupling. Both interaction types lead to a shift of the ^{31}P resonance frequency, although the pseudo-contact shift due to electron–nuclear dipolar interactions was observed to be a lot smaller than the Fermi contact shift in related olivine-type LiTMPO$_4$ (TM = Fe, Mn, Co)[46-48] such that the overall chemical shift can be approximated by the Fermi contact shift (δ_{FC}) here. A fit of the ^{31}P spectrum of KVPO$_4$F indicates two broad ^{31}P resonances at ~4600 and ~3400 ppm, consistent with the presence of two P crystallographic sites (P1 and P2) in the structure. To assist in the assignment of the ^{31}P NMR spectrum of KVPO$_4$F, hybrid DFT/ HF calculations of the ^{31}P NMR parameters were performed on a fully optimized KVPO$_4$F structure (after relaxation of the atomic positions and lattice parameters) using two hybrid functionals with 20% (HYB20) and 35% (HYB35) HF exchange. The comparison of the experimental spectrum and first-principles results in Supplementary Table 4 indicates an ~1200- ppm shift difference between the two experimental peaks, which is in good agreement with the difference between the Fermi contact shifts computed for P1 and P2 ($\Delta\delta_{FC}$), ranging from 1187 ppm (HYB35 calculations) to 1471 ppm (HYB20 calculations). We note that the shifts and shift differences obtained using the HYB35 functional are in better agreement with the experimental data than those obtained with HYB20; however, the absolute δ_{FC} values computed for P1 and P2 are still larger than those observed experimentally by at least ~800 ppm. This discrepancy may be attributed to spin-orbit coupling resulting from the non-zero orbital angular momentum of V^{3+} ($t_{2g}^2 e_g^0$ electronic configuration), not accounted for in our NMR calculations. Spin-orbit coupling leads to both g-tensor anisotropy and zero field splitting and affects the δ_{FC}. It was recently demonstrated that spin-orbit coupling corrections (via the isotropic g shift) to the δ_{FC} of ^{31}P in olivine-type LiFePO$_4$ ($t_{2g}^4 e_g^2$), LiCoPO$_4$ ($t_{2g}^5 e_g^2$), LiNiPO$_4$ ($t_{2g}^6 e_g^2$) are comprised

between ~800 ppm and ~1400 ppm, while the δ_{FC} itself is comprised between ~1600 and ~3200 ppm.[48] Hence, it is not unlikely that corrections of a similar order of magnitude may need to be applied to our calculation results on $KVPO_4F$, but this should not significantly affect the shift differences $\Delta\delta_{FC}$ in Supplementary Table 4. Our calculations indicate a larger shift for P1 than for P2, leading us to assign the ~4600 ppm peak to P1 and the ~3400 ppm peak to P2. We note that anisotropic electron–nuclear dipolar interactions are only partially averaged out by fast spinning of the powder sample at the MAS and result in additional peaks (sidebands) in the ^{31}P NMR spectrum obtained for $KVPO_4F$, as indicated by the asterisk. The sharp signal at 0 ppm is attributed to a diamagnetic impurity present in both $KVPO_4F$ and $KVPO_{4.26}F_{0.64}$.

The ^{31}P spectrum of $KVPO_{4.36}F_{0.64}$ exhibits more resonances than that of $KVPO_4F$, indicating a larger number of effective P environments in the material. Although all the P sites are surrounded by four V^{3+} in their first metal coordination shell in $KVPO_4F$, partial oxidation of V in $KVPO_{4.36}F_{0.64}$ can create additional P environments surrounded by (1) three V^{3+} and one V^{4+}, (2) two V^{3+} and two V^{4+}, (3) one V^{3+} and three V^{4+}, or (4) V^{4+} only in the first metal coordination shell. Because V^{3+} and V^{4+} lead to different shift contributions to the total ^{31}P paramagnetic shift and because the individual contributions from the four V in the first coordination shell are additive, the progressive oxidation of one, two, three, and four V^{3+} to V^{4+} in the first metal coordination shell of P results in discrete changes in the two resonant frequencies observed in the $KVPO_4F$ spectrum. In fact, the resonances observed at ~5400, ~4600, ~3400, ~2200, and ~1200 ppm in the $KVPO_{4.36}F_{0.64}$ spectrum are almost all separated by ~1200 ppm, suggesting that these different resonances correspond to P environments surrounded by varying numbers of V^{3+} and V^{4+} cations in the first metal coordination shell. We speculate that fewer unpaired electrons for V^{4+} result in a smaller shift contribution than for V^{3+} and tentatively assign the higher resonant frequencies (5400 and 4600 ppm) to P local environments with a majority of V^{3+} neighbors. In contrast, the lower resonant frequencies

12

(2200 and 1200 ppm) likely correspond to P sites with mostly V^{4+} neighbors. Furthermore, the broad peaks at 5400, 4600, 3400, 2200, and 1200 ppm in the $KVPO_{4.36}F_{0.64}$ ^{31}P NMR spectrum correspond to overlapping signals from ^{31}P sites with a particular V^{3+}/V^{4+} metal coordination (as discussed above) but with slightly different V–O, V–F, O–P, and F–P bond lengths and V–O–P and V–F–P bond angles, leading to slightly different resonant frequencies. Unlike for $KVPO_4F$, spinning sidebands cannot be distinguished in the spectrum obtained for $KVPO_{4.36}F_{0.64}$ because of the large number of P signals and the broad, overlapping resonances. Overall, the ^{31}P NMR data indicate a more disordered structure for $KVPO_{4.36}F_{0.64}$ than for $KVPO_4F$ with a larger range of bond distances and bond angles and a greater number of local P environments with various numbers of V^{3+} and V^{4+} cations in the first metal coordination shell.

Figure 7a shows the galvanostatic charge/discharge profiles of $KVPO_4F$ and $KVPO_{4.36}F_{0.64}$ in the second cycle at a current rate of 5 mA g^{-1}. $KVPO_{4.36}F_{0.64}$ delivers a reversible capacity of ~85 mAh g^{-1} with an average discharge voltage of ~4.2 V. In contrast, $KVPO_4F$ provides a reversible specific capacity of ~100 mAh g^{-1} and an average discharge voltage of ~4.3 V. The smaller capacity of $KVPO_{4.36}F_{0.64}$ than $KVPO_4F$ is attributable to its higher average V oxidation state in $KVPO_{4.36}F_{0.64}$ than in $KVPO_4F$which leaves less V^{3+} to be oxidized. . The lower F concentration also results in a lower working voltage for $KVPO_{4.36}F_{0.64}$ than for $KVPO_4F$ likely because of the reduced inductive effect.[32] The differences in the voltage curves of the two materials are highlighted in Figure 7b: the voltage profiles of $KVPO_4F$ and $KVPO_{4.36}F_{0.64}$ are replotted as a function of relative capacity normalized by the obtained capacities. $KVPO_4F$ exhibits multiple plateaus, whereas the voltage profile of $KVPO_{4.36}F_{0.64}$ is smooth without plateau-like features. This difference reflects the disordered local structure in $KVPO_{4.36}F_{0.64}$, as revealed by ^{31}P NMR (Figure 6c). To obtain a better understanding of the effect of oxygenation in $KVPO_4F$ on its local structure, we predict the most stable structures of $KVPO_4F$ and $KVPO_{4.375}F_{0.625}$ using DFT calculations. Here, we calculated the structure of

$KVPO_{4.375}F_{0.625}$, which has a composition similar to that of $KVPO_{4.36}F_{0.64}$ with a reasonable unit cell size. Supplementary Figure 8 and 9 show the local K and V environments in $KVPO_4F$ and $KVPO_{4.375}F_{0.625}$, respectively. As mentioned previously, $KVPO_4F$ exhibits two 9-coordinate K sites with local coordination KO_7F_2 and two octahedral V sites with coordination VO_4F_2. In contrast, $KVPO_{4.375}F_{0.625}$ has a greater range of K and V environments: three 9-coordinate K sites with local coordination of one KO_7F_2, one KO_8F, and one KO_9 and four octahedral V sites with local coordination including two VO_4F_2, one VO_5F, and one VO_6. The various K and V sites present in the $KVPO_{4.375}F_{0.625}$ structure can lead to more continuous energy changes upon K extraction, which can be translated into a more sloped voltage profile compared with that for $KVPO_4F$.

3. Discussion

Layered $K\text{-}TMO_2$ compounds exhibit sloped voltage curves upon charge and discharge because the two-dimensional arrangement of large K ions in the alkali metal layer leads to short K^+–K^+ distances, resulting in strong interaction between the K ions.[16, 19] For example, the extraction of 0.33 K^+ from $K_{0.6}CoO_2$ leads to a voltage change of 2.2 V, *i.e.,* the average voltage slope is 6.67 V per 1 K^+ transfer.[16] Similarly, 0.45 K^+ can be extracted from the $K_{0.5}MnO_2$ cathode as the potential is increased by 2.4 V, corresponding to an average voltage slope of 5.33 V per 1 K^+ transfer.[19] Supplementary Figure 10 presents a simplified schematic of the voltage curves of $K\text{-}TMO_2$ compounds with different voltage slopes. Within a reasonable voltage window (4.0–1.5 V) and considering the stability range of layered K-TMO_2 upon K extraction, the achievable specific capacity substantially depends on the average slope of the voltage *vs.* capacity profile. In addition, the sloped voltage curves generally lead to an average voltage lower than 3.0 V in the range of 4.0–1.5 V (*vs.* K/K^+), as observed in the plot. Overall, the large slopes of the $K\text{-}TMO_2$ voltage curves limit both the achievable specific capacity and voltage and, therefore, the energy density of these materials. In contrast, ~1.0 K^+ can be extracted from $KVPO_4F$ in the voltage range of ~1.0 V. In this

14

case, the average voltage slope is ~1 V per 1 K^+ transfer, which is 5–7 times smaller than the slopes of reported layered K-TMO$_2$ compounds. This finding suggests that the K^+–K^+ interactions in KVPO$_4$F are substantially weaker than those in the layered K-TMO$_2$ compounds because of the three-dimensional arrangement of K ions in the fluorophosphate framework that allows for a longer K^+–K^+ distance (~3.8 Å in KVPO$_4$F $vs.$ ~2.8 Å in $K_{0.6}CoO_2$).[16] The size of the voltage steps in the electrochemical curve is another indicator of the strength of the K^+–K^+ interactions in the host material. K_xVPO_4F exhibits a voltage step of ~0.35 V at x = 0.5, whereas a much larger voltage step of ~0.5 V is observed for K_xCoO_2 at the same K content,[16] confirming the smaller K^+ interaction in KVPO$_4$F than in layered K-TMO$_2$. As a result, the KVPO$_4$F cathode delivers a respectable capacity of 105 mAh g^{-1} with an exceptionally high discharge voltage of ~4.33 V ($vs.$ K/K$^+$), thereby providing a high gravimetric energy density of 454 Wh kg^{-1}. This is remarkably larger than that of layered K-TMO$_2$ compounds (see Figure 3). Overall, this study demonstrates that KVPO$_4$F with a polyanionic framework can provide a higher working voltage and exhibits a voltage curve with a smaller slope than that of layered K-TMO$_2$ compounds. In this respect, our work demonstrates that it is crucial to explore new cathode materials with polyanionic frameworks for KIBs, as they can provide a high working voltage and, thus, a high energy density.

The stoichiometric KVPO$_4$F exhibits multiple plateaus as K is extracted because of the formation of the stable intermediate phases at x = 0.75, 0.625, and 0.5 in K_xVPO_4F (Figure 4 and 5). The formation of intermediate phases is attributable to the formation of K^+/vacancy orderings at specific K contents to reduce the strength of K^+–K^+ interactions. Oxygen substitution for fluorine in KVPO$_4$F is effective in reducing K^+/vacancy ordering because the locally disordered fluorine–oxygen anion distribution makes the K site energies different, disrupting the K^+/vacancy ordering. Therefore, the oxygenation will wipe out the voltage steps from the KVPO$_{4+x}$F$_{1-x}$ cathode, as shown in Figure 7. In fact, the shape of the voltage curve of our non-stoichiometric KVPO$_{4.36}$F$_{0.64}$ is almost identical to that reported by Chihara

et al.[33] These findings strongly suggest that their material is likely the anion-disordered $KVPO_{4+x}F_{1-x}$ compound rather than stoichiometric $KVPO_4F$. In addition, the refinement results obtained by Chihara *et al.* indicate that the bond valence sums of V1 and V2 are +3.2 and +3.4, respectively, presumably due to partial oxygenation. As a result, their compound delivers ~80 mAh g^{-1} with an average voltage of ~4.1 V,[33] similar to the properties of our oxygen-substituted $KVPO_{4.36}F_{0.64}$. Consequently, we argue that the synthesis of stoichiometric $KVPO_4F$ needs to be delicately tuned to achieve high energy density.

4. Conclusion

In this study, stoichiometric $KVPO_4F$ was synthesized and evaluated as a cathode material for KIBs. The $KVPO_4F$ cathode delivers a reversible capacity of ~105 mAh g^{-1} with an average voltage of ~4.33 V (*vs.* K/K$^+$), resulting in a gravimetric energy density of ~454 Wh kg^{-1}. Reversible K extraction from and reinsertion into K_xVPO_4F is confirmed by *ex situ* XRD characterization combined with DFT calculations, revealing the formation of stable intermediate compounds at $x = 0.75$, 0.625, and 0.5. This work further explains how the F/O ratio in $KVPO_{4+x}F_{1-x}$ affects its electrochemical properties. The oxygenation of $KVPO_4F$ leads to a more disordered structure around the K and V sites and thus a smooth voltage profile without voltage plateaus. In addition, oxygen substitution for fluorine in $KVPO_4F$ reduces the achievable specific capacity as well as the operating voltage. These effects can be explained by partial V^{3+} oxidation in the oxygenated compound and by a reduced inductive effect as the F content is decreased, respectively.

5. Experimental Section

Synthesis of stoichiometric KVPO₄F and non-stoichiometric KVPO₄.₃₆F₀.₆₄

$KVPO_4F$ was prepared using a two-step reaction. In the first step, VPO_4 was synthesized by reacting $NH_4H_2PO_4$ (11.5 g, 98%, Alfa Aesar), V_2O_5 (9.05 g, >99.6%, Sigma–Aldrich), and carbon black (1.2 g, super P, Timcal). The precursors were mixed using a wet ball-milling method with zirconia balls and an acetone solvent in a polypropylene jar for 12 h and then

dried overnight at 100 ºC. The mixture was pelletized and then sintered at 750 ºC for 4 h with Ar flow. In the second step, stoichiometric amounts of KF (99.9%, Sigma–Aldrich) and VPO_4 were homogeneously mixed using a planetary ball mill (Retsch PM200) at 300 rpm for 4 h. The powder was then pelletized and sintered at 650 ºC for 8 h with Ar flow. The carbon black was used as a reducing agent to control the fluorophosphate stoichiometry, ensuring the trivalency of V. Non-stoichiometric $KVPO_{4.36}F_{0.64}$ was prepared using a similar process as $KVPO_4F$ but without carbon, and the nominal composition was determined using inductively coupled plasma technique (Luvak, USA). For the synthesis of $KVPO_{4.36}F_{0.64}$, VPO_4 and KF (99.9%, Sigma–Aldrich) were homogeneously mixed using a planetary ball mill (Retsch PM200) at 300 rpm for 4 h. The mixture was pelletized and then sintered at 600 ºC for 1 h with flow of a $H_2(2\%)/Ar(98\%)$ mixture gas.

Electrochemical measurements

Electrodes were prepared by mixing the active material ($KVPO_4F$ or $KVPO_{4.36}F_{0.64}$) (80 wt%), Super P carbon black (Timcal, 10 wt%), and PTFE (DuPont, 10 wt%) binder in an Ar-filled glovebox. Test cells were assembled into 2032 coin-cells in the glovebox with a two-electrode configuration using K-metal counter electrodes. A separator of grade GF/F (Whatman, USA) and an electrolyte of 0.7 M KPF_6 in ethylene carbonate/diethyl carbonate (EC/DEC; anhydrous, 1:1 volume ratio) were used. The electrochemical tests were performed using a battery testing station (BT-2000, Arbin Instruments) with cathode films with a loading density of ~5.1 mg cm^{-2}.

Synchrotron-based X-ray diffraction analysis

High-resolution synchrotron powder diffraction data were collected at beamline 11-BM at the Advanced Photon Source (APS), Argonne National Laboratory, using an average wavelength of 0.457 Å. Discrete detectors covering an angular range from −6° to 16° 2θ were scanned over a 34° 2θ range, with data points collected every 0.001° 2θ and a scan speed of 0.01°/s. The samples were sealed in polyimide (Kapton, Cole-Parmer) capillaries and measured for 1

h. Rietveld refinement[49] of the data was performed using the Fullprof program,[50] and structure visualization was performed with VESTA.[51]

X-ray absorption near-edge structure analysis

Vanadium K-edge X-ray absorption near-edge structure (XANES) experiments were performed in transmission mode at room temperature in an Ar gas-ionization chamber using a Si(111) double-crystal monochromator detuned to ~70% of its original intensity to eliminate higher-order harmonics at the 10C beamline at Pohang Light Sources-II (PLS-II). A reference spectrum of V metallic foil was collected simultaneously for the energy calibration. The XANES data were handled and processed using the Athena program.

Magnetic susceptibility measurements

Field-cooled (FC) and zero-field-cooled (ZFC) DC magnetic susceptibility data of the as-synthesized $KVPO_4F$ were recorded using a commercial magnetic property measurement system (MPMS) over the temperature range of 2 K to 390 K under an external field of 1000 Oe.

^{31}P NMR analysis

^{31}P NMR data were obtained at room temperature using a Bruker Avance 500 MHz (11.7 T) wide-bore NMR spectrometer at a Larmor frequency of 202.5 MHz. The data were obtained under 60-kHz magic angle spinning (MAS) using a 1.3-mm double-resonance probe. The ^{31}P chemical shifts were referenced against phosphoric acid (85 wt% H_3PO_4 in a deuterated solution, $\delta = 0$ ppm). To effectively excite the broad range of ^{31}P resonant frequencies present in paramagnetic $KVPO_4F$ and $KVPO_{4.36}F_{0.64}$, a double-adiabatic spin-echo experiment, previously used on closely related $LiFe_xMn_{1-x}PO_4$ compounds,[46] was conducted. This pulse sequence employs a pair of tanh/tan short high-power adiabatic pulses (SHAPs),[52] each sweeping through a 5-MHz frequency range in 50 μs with an RF amplitude of 312.5 kHz (300 W). The double-adiabatic spin-echo spectra were obtained using a 90° RF pulse of 0.8 μs at 300 W, followed by two high-power 180° SHAPs described above. A recycle delay of 0.1 s

was used throughout the experiment. Lineshape analysis was performed using the SOLA lineshape simulation package within the Bruker Topspin software.

Hybrid DFT/HF calculations of paramagnetic NMR parameters

Spin-unrestricted hybrid density functional theory/Hartree Fock (DFT/HF) calculations were performed on stoichiometric $KVPO_4F$, starting from the structure obtained from Rietveld refinement and reported in Supplementary Table 1. The CRYSTAL14 all-electron linear combination of atomic orbitals (LCAO) code[53] was used, and two spin-polarized exchange-correlation functionals based upon the B3LYP form were applied, with weights of the HF exchange of 20% (B3LYP or H20) and 35% (H35). Electron-nuclear hyperfine NMR parameters were obtained in ferromagnetically aligned cells (at 0 K) using a method identical to that described elsewhere.[47, 54] Briefly, the Fermi contact shift (δ_{FC}) is computed from the spin density at the nuclear position. δ_{FC} is subsequently scaled to a value consistent with the room-temperature paramagnetic state in which the experiments were performed by multiplication with the so-called magnetic scaling factor Φ:[54]

$$\Phi(T) = \frac{B_0 \mu_{eff}^2}{3 k_B g_e \mu_B S(T - \Theta)}.$$

Here, B_0 is the external magnetic field strength, μ_{eff} is the effective magnetic moment per V site, k_B is Boltzmann's constant, g_e is the electron g-factor, μ_B is the Bohr magneton, S is the formal spin of the transition metal species ($S_{V^{3+}} = 1$), T is the temperature of the sample (assumed to be 320 K to account for frictional heating caused by fast (60-kHz) rotation of the NMR rotor), and Θ is the Weiss constant. μ_{eff} and Θ were determined from magnetic susceptibility measurements of the as-synthesized stoichiometric $KVPO_4F$. The Θ and μ_{eff} values used to compute the scaling factor Φ are the average values determined from the FC and ZFC data obtained on the as-synthesized $KVPO_4F$: $\Theta = 6 \pm 3$ K and $\mu_{eff} = \sqrt{8 \times C} = 2.55 \, \mu_B$, where C is the Curie constant. Using the equation above, the

scaling factor at 320 K is $\Phi(320K) = 0.0262.$ Full details of the calculations, including the basis sets and numerical parameters, are provided in the Supplementary Information.

DFT calculation of phase stability and voltage profile

First-principles DFT calculations on K_xVPO_4F were performed with the spin-polarized generalized gradient approximation (GGA) using the Perdew–Burke–Ernzerhof (PBE) exchange-correlation functional.[55] The projector augmented-wave approach[56] was used as implemented in the Vienna *ab initio* simulation package (VASP).[57] The Hubbard U correction to GGA (GGA+U) was employed to correct the self-interaction error of GGA.[58] A U value of 4 eV was used for V, as employed in previous computational studies of vanadium fluorophosphates.[59-60] A plane-wave energy cutoff of 520 eV and a *gamma*-centered $3 \times 2 \times 2$ *k*-point grid were used. All symmetric distinct K-vacancy orderings within the unit cell of K_xVPO_4F including 8 formula units were generated using the enumeration technique reported by Hart *et al.*,[39] and the 50 configurations with the lowest electrostatic energy at each K content were calculated using GGA+U. The voltage profile was calculated from the DFT energies of the most stable configurations at each K content as[61]

$$V = -\frac{E(K_{x2}VPO_4F) - E(K_{x1}VPO_4F) - (x_2 - x_1)E(K)}{(x_2 - x_1)F},$$

where $E(K_xVPO_4F)$ and $E(K)$ are the DFT energies of the most stable K_xVPO_4F and bcc K metal (space group: Im-3m), respectively, and *F* is the Faraday constant. To find reasonable configurations for $KVPO_{4.375}F_{0.625}$, all fluorine–oxygen orderings for additional oxygen at F sites of $KVPO_4F$ were generated using the same enumeration technique as previously discussed, and the 10 configurations with lowest electrostatic energy were calculated using GGA+U.

Supporting Information

Supporting Information is available from the Wiley Online Library or from the author.

References

[1] S. P. ATACAMA, *The Economist* **2016 Jan. 14th**.

[2] E. A. Olivetti, G. Ceder, G. G. Gaustad, X. Fu, *Joule* **2017**, *1*, 229.

[3] S.-W. Kim, D.-H. Seo, X. Ma, G. Ceder, K. Kang, *Adv. Energy Mater.* **2012**, *2*, 710.

[4] H. Kim, H. Kim, Z. Ding, M. H. Lee, K. Lim, G. Yoon, K. Kang, *Adv. Energy Mater.* **2016**, *6*, 1600943.

[5] H. Kim, J. C. Kim, M. Bianchini, D.-H. Seo, J. Rodriguez-Garcia, G. Ceder, *Adv. Energy Mater.*, DOI: 10.1002/aenm.2017023841702384.

[6] J. C. Pramudita, D. Sehrawat, D. Goonetilleke, N. Sharma, *Adv. Energy Mater.* **2017**, *7*, 1602911.

[7] X. Wu, D. P. Leonard, X. Ji, *Chem. Mater.* **2017**, *29*, 5031.

[8] S. Komaba, T. Hasegawa, M. Dahbi, K. Kubota, *Electrochem. Commun,* **2015**, *60*, 172.

[9] W. Luo, J. Wan, B. Ozdemir, W. Bao, Y. Chen, J. Dai, H. Lin, Y. Xu, F. Gu, V. Barone, L. Hu, *Nano Lett.* **2015**, *15*, 7671.

[10] G. Yoon, H. Kim, I. Park, K. Kang, *Adv. Energy Mater.* **2017**, *7*, 1601519.

[11] H. Kim, J. Hong, Y.-U. Park, J. Kim, I. Hwang, K. Kang, *Adv. Funct. Mater.* **2015**, *25*, 534.

[12] H. Kim, J. Hong, G. Yoon, H. Kim, K.-Y. Park, M.-S. Park, W.-S. Yoon, K. Kang, *Energy Environ. Sci.* **2015**, *8*, 2963.

[13] M. S. Whittingham, *Chem. Rev.* **2004**, *104*, 4271.

[14] M. H. Han, E. Gonzalo, G. Singh, T. Rojo, *Energy Environ. Sci.* **2015**, *8*, 81.

[15] P. Vassilaras, S. T. Dacek, H. Kim, T. T. Fister, S. Kim, G. Ceder, J. C. Kim, *J. Electrochem. Soc.* **2017**, *164*, A3484.

[16] H. Kim, J. C. Kim, S.-H. Bo, T. Shi, D.-H. Kwon, G. Ceder, *Adv. Energy Mater.* **2017**, *7*, 1700098.

[17] Y. Hironaka, K. Kubota, S. Komaba, *Chem. Commun.* **2017**, *53*, 3693.

[18] C. Vaalma, G. A. Giffin, D. Buchholz, S. Passerini, *J. Electrochem. Soc.* **2016**, *163*, A1295.

[19] H. Kim, D.-H. Seo, J. C. Kim, S.-H. Bo, L. Liu, T. Shi, G. Ceder, *Adv. Mater.* **2017**, *29*, 1702480.

[20] X. Wang, X. Xu, C. Niu, J. Meng, M. Huang, X. Liu, Z. Liu, L. Mai, *Nano Lett.* **2017**, *17*, 544.

[21] C. Liu, S. Luo, H. Huang, Z. Wang, A. Hao, Y. Zhai, Z. Wang, *Electrochem. Commun,* **2017**, *82*, 150.

[22] J. Han, G.-N. Li, F. Liu, M. Wang, Y. Zhang, L. Hu, C. Dai, M. Xu, *Chem. Commun.* **2017**, *53*, 1805.

[23] N. Recham, G. Rousse, M. T. Sougrati, J.-N. Chotard, C. Frayret, S. Mariyappan, B. C. Melot, J.-C. Jumas, J.-M. Tarascon, *Chem. Mater.* **2012**, *24*, 4363.

[24] W. B. Park, S. C. Han, C. Park, S. U. Hong, U. Han, S. P. Singh, Y. H. Jung, D. Ahn, K.-S. Sohn, M. Pyo, *Adv. Energy Mater.*, DOI: 10.1002/aenm.2017030991703099.

[25] R. K. B. Gover, P. Burns, A. Bryan, M. Y. Saidi, J. L. Swoyer, J. Barker, *Solid State Ionics* **2006**, *177*, 2635.

[26] J. Barker, R. K. B. Gover, P. Burns, A. Bryan, M. Y. Saidi, J. L. Swoyer, *J. Power Sources* **2005**, *146*, 516.

[27] Y. Lu, S. Zhang, Y. Li, L. Xue, G. Xu, X. Zhang, *J. Power Sources* **2014**, *247*, 770.

[28] T. Jin, Y. Liu, Y. Li, K. Cao, X. Wang, L. Jiao, *Adv. Energy Mater.* **2017**, *7*, 1700087.

[29] N. R. Khasanova, O. A. Drozhzhin, D. A. Storozhilova, C. Delmas, E. V. Antipov, *Chem. Mater.* **2012**, *24*, 4271.

[30]   S.-W. Kim, D.-H. Seo, H. Kim, K.-Y. Park, K. Kang, *Phys. Chem. Chem. Phys.* **2012**, *14*, 3299.

[31]   S. S. Fedotov, N. R. Khasanova, A. S. Samarin, O. A. Drozhzhin, D. Batuk, O. M. Karakulina, J. Hadermann, A. M. Abakumov, E. V. Antipov, *Chem. Mater.* **2016**, *28*, 411.

[32]   M. Prabu, M. V. Reddy, S. Selvasekarapandian, G. V. S. Rao, B. V. R. Chowdari, *Electrochim. Acta* **2012**, *85*, 572.

[33]   K. Chihara, A. Katogi, K. Kubota, S. Komaba, *Chem. Commun.* **2017**, *53*, 5208.

[34]   L. Xue, Y. Li, H. Gao, W. Zhou, X. Lü, W. Kaveevivitchai, A. Manthiram, J. B. Goodenough, *J. Am. Chem. Soc.* **2017**, *139*, 2164.

[35]   C. Deng, S. Zhang, B. Zhao, *Energy Storage Mater.* **2016**, *4*, 71.

[36]   J. Kim, I. Park, H. Kim, K.-Y. Park, Y.-U. Park, K. Kang, *Adv. Energy Mater.* **2016**, *6*, 1502147.

[37]   R. A. Shakoor, D.-H. Seo, H. Kim, Y.-U. Park, J. Kim, S.-W. Kim, H. Gwon, S. Lee, K. Kang, *J. Mater. Chem.* **2012**, *22*, 20535.

[38]   M. Xu, C.-J. Cheng, Q.-Q. Sun, S.-J. Bao, Y.-B. Niu, H. He, Y. Li, J. Song, *RSC Adv.* **2015**, *5*, 40065.

[39]   G. L. W. Hart, R. W. Forcade, *Phys. Rev. B* **2008**, *77*, 224115.

[40]   Y. Hinuma, Y. S. Meng, G. Ceder, *Phys. Rev. B* **2008**, *77*, 224111.

[41]   V. L. Chevrier, S. P. Ong, R. Armiento, M. K. Y. Chan, G. Ceder, *Phys. Rev. B* **2010**, *82*, 075122.

[42]   J. C. Kim, D.-H. Seo, G. Ceder, *Energy Environ. Sci.* **2015**, *8*, 1790.

[43]   D. Wang, X. Wu, Z. Wang, L. Chen, *J. Power Sources* **2005**, *140*, 125.

[44]   J.-M. Ateba Mba, C. Masquelier, E. Suard, L. Croguennec, *Chem. Mater.* **2012**, *24*, 1223.

[45]   E. Boivin, J.-N. Chotard, M. Ménétrier, L. Bourgeois, T. Bamine, D. Carlier, F. Fauth, C. Masquelier, L. Croguennec, *J. Phys. Chem. C* **2016**, *120*, 26187.

[46]   R. J. Clément, A. J. Pell, D. S. Middlemiss, F. C. Strobridge, J. K. Miller, M. S. Whittingham, L. Emsley, C. P. Grey, G. Pintacuda, *J. Am. Chem. Soc.* **2012**, *134*, 17178.

[47]   D. S. Middlemiss, A. J. Ilott, R. J. Clément, F. C. Strobridge, C. P. Grey, *Chem. Mater.* **2013**, *25*, 1723.

[48]   R. Pigliapochi, A. J. Pell, I. D. Seymour, C. P. Grey, D. Ceresoli, M. Kaupp, *Phys. Rev. B* **2017**, *95*, 054412.

[49]   H. Rietveld, *J. Appl. Crys.* **1969**, *2*, 65.

[50]   J. Rodríguez-Carvajal, *Physica B: Condensed Matter* **1993**, *192*, 55.

[51]   K. Momma, F. Izumi, *J. Appl. Crys.* **2011**, *44*, 1272.

[52]   G. Kervern, G. Pintacuda, L. Emsley, *Chem. Phys. Lett.* **2007**, *435*, 157.

[53]   R. Dovesi, R. Orlando, A. Erba, C. M. Zicovich‐Wilson, B. Civalleri, S. Casassa, L. Maschio, M. Ferrabone, M. D. L. Pierre, P. D'Arco, Y. Noël, M. Causà, M. Rérat, B. Kirtman, *Int. J. Quantum Chem.* **2014**, *114*, 1287.

[54]   J. Kim, D. S. Middlemiss, N. A. Chernova, B. Y. X. Zhu, C. Masquelier, C. P. Grey, *J. Am. Chem. Soc.* **2010**, *132*, 16825.

[55]   J. P. Perdew, *Phys. Rev. Lett.* **1996**, *77*, 3865.

[56]   P. E. Blöchl, *Phys. Rev. B* **1994**, *50*, 17953.

[57]   G. Kresse, *Comput. Mater. Sci.* **1996**, *6*, 15.

[58]   S. L. Dudarev, G. A. Botton, S. Y. Savrasov, C. J. Humphreys, A. P. Sutton, *Phys. Rev. B* **1998**, *57*, 1505.

[59]   Y. U. Park, D. H. Seo, H. Kim, J. Kim, S. Lee, B. Kim, K. Kang, *Adv. Funct. Mater.* **2014**, *24*, 4603.

[60]   M. Bianchini, P. Xiao, Y. Wang, G. Ceder, *Adv. Energy Mater.* **2017**, *7*, 1700514.

[61]   M. K. Aydinol, A. F. Kohan, G. Ceder, K. Cho, J. Joannopoulos, *Phys. Rev. B* **1997**, *56*, 1354.
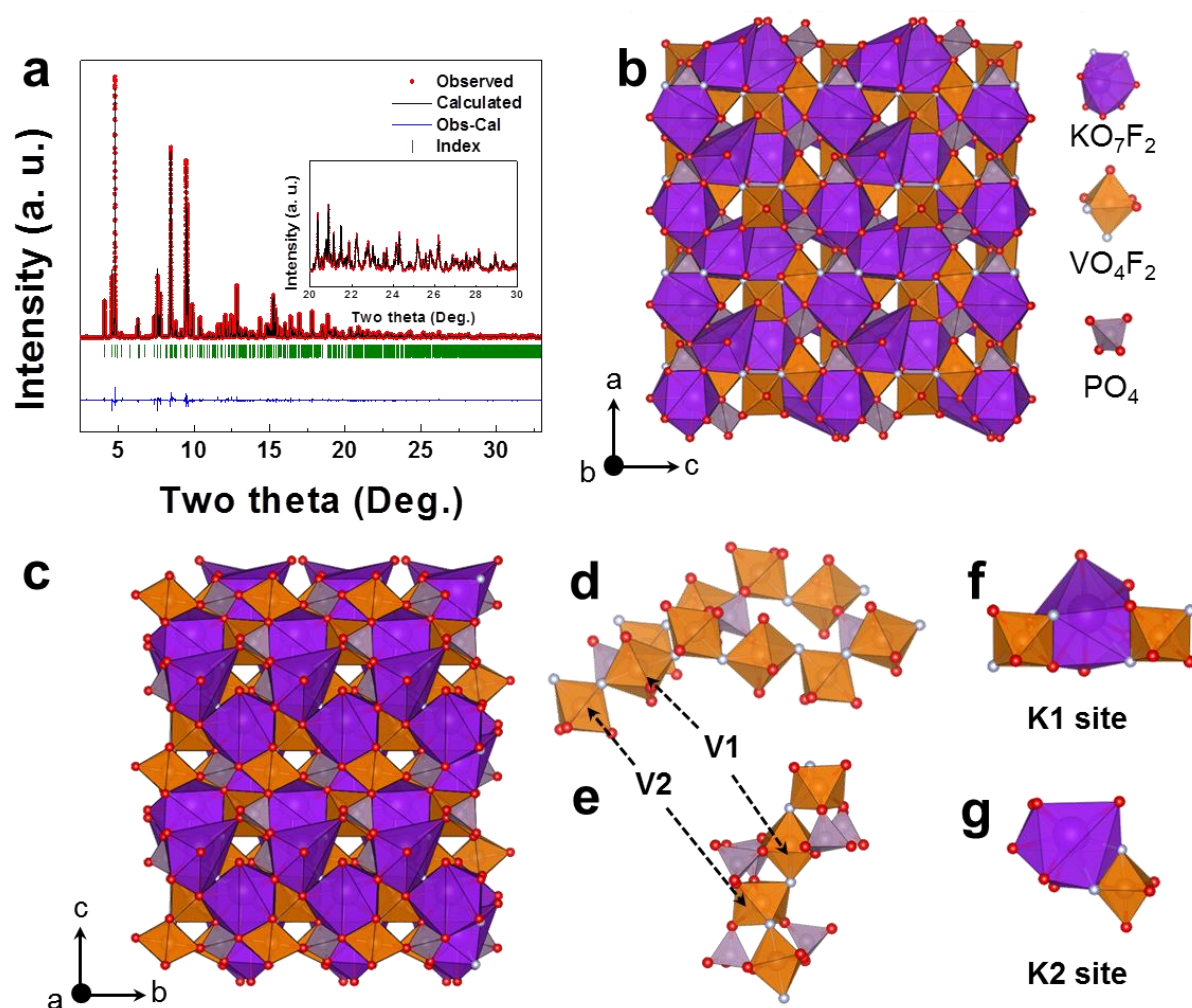
Figure 1. Structural analysis of KVPO$_4$F. a. Rietveld refinement of X-ray diffraction pattern of KVPO$_4$F (wavelength = 0.457 Å). (Inset: Enlarged X-ray diffraction pattern from 20º to 30º.) The crystal structure of KVPO$_4$F projected along **b.** *b*-axis and **c.** *a*-axis. **d.** Connectivity of vanadium octahedrons. **e.** Local vanadium octahedral environment. **f.** K1 site and **g.** K2 site.
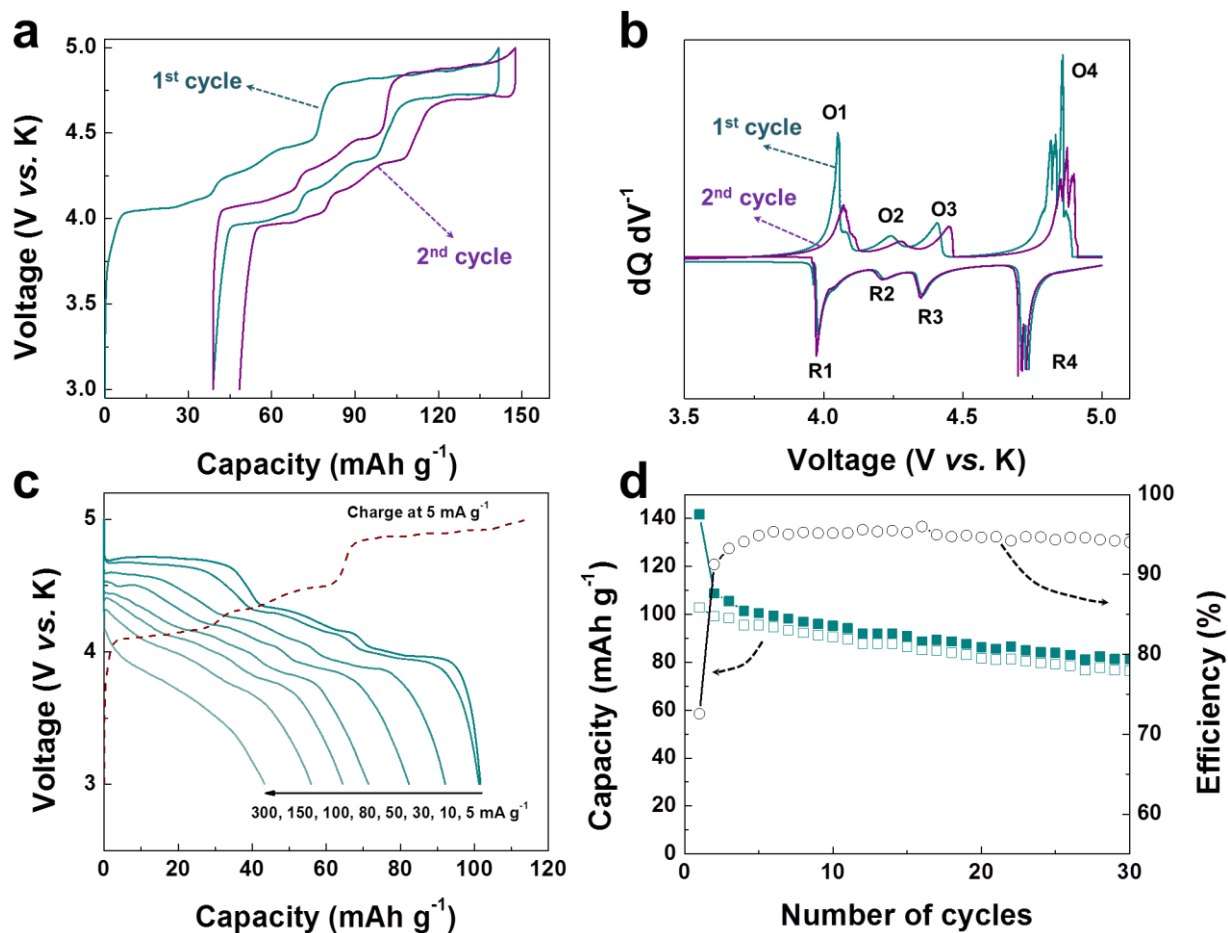
Figure 2. K-storage properties of KVPO$_4$F cathode. a. Charge/discharge profiles of KVPO$_4$F at 5 mA g^{-1}. **b.** Differential capacity (dQ dV^{-1}) curves of KVPO$_4$F for 1st and 2nd cycles. **c.** Rate capability of KVPO$_4$F at various current densities ranging from 5 to 300 mA g^{-1}. **d.** Capacity retention of KVPO$_4$F at 5 mA g^{-1}.
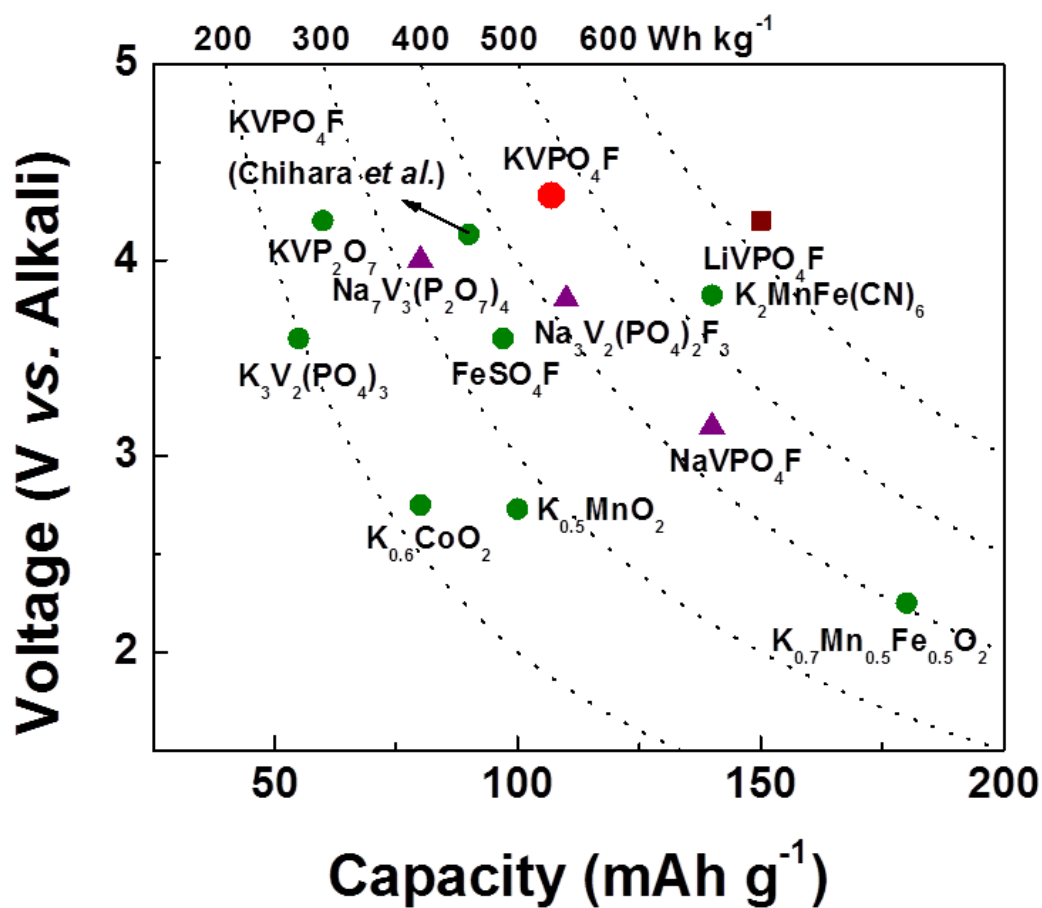
Figure 3. Performance comparison of KVPO₄F and various cathode materials for LIBs, NIBs, and KIBs. Capacity–voltage plots of various cathode materials for LIBs, NIBs, and KIBs. Here, the plotted voltages are the average experimental discharge voltages reported in the literature.[16, 19-20, 22-24, 26, 33-38] (Green: KIB cathodes, Purple: NIB cathodes, Brown: LIB cathodes, and Red: KVPO₄F)
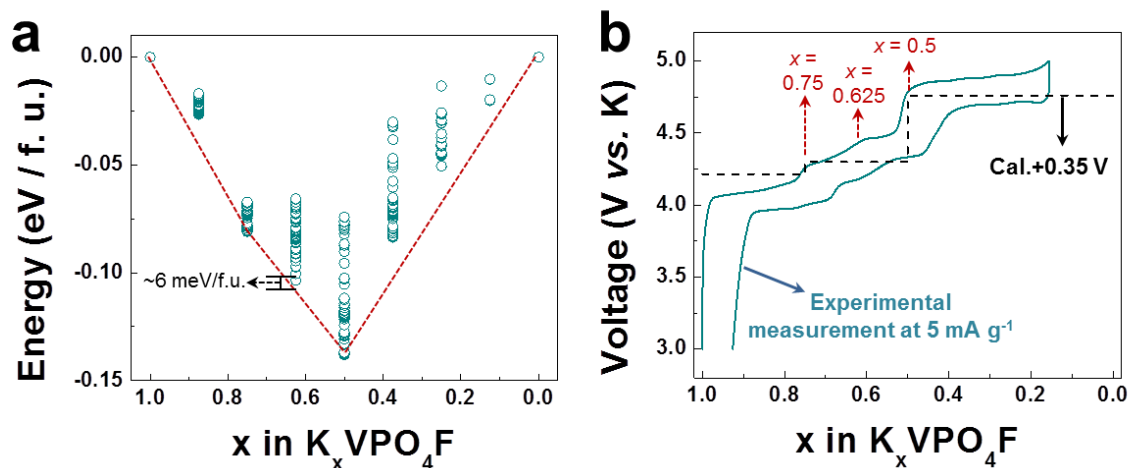
Figure 4. **a.** Formation energy of K_xVPO_4F as a function of K content (*x*) obtained using first-principles DFT calculations. **b.** Calculated voltage plot (dashed line) compared with experimentally obtained charge/discharge profiles (solid line). The red dashed line in (a) is the convex hull of the formation energy. We note that the calculated voltage plot is shifted upwards by 0.35 V for better agreement with the experimental voltage curve.
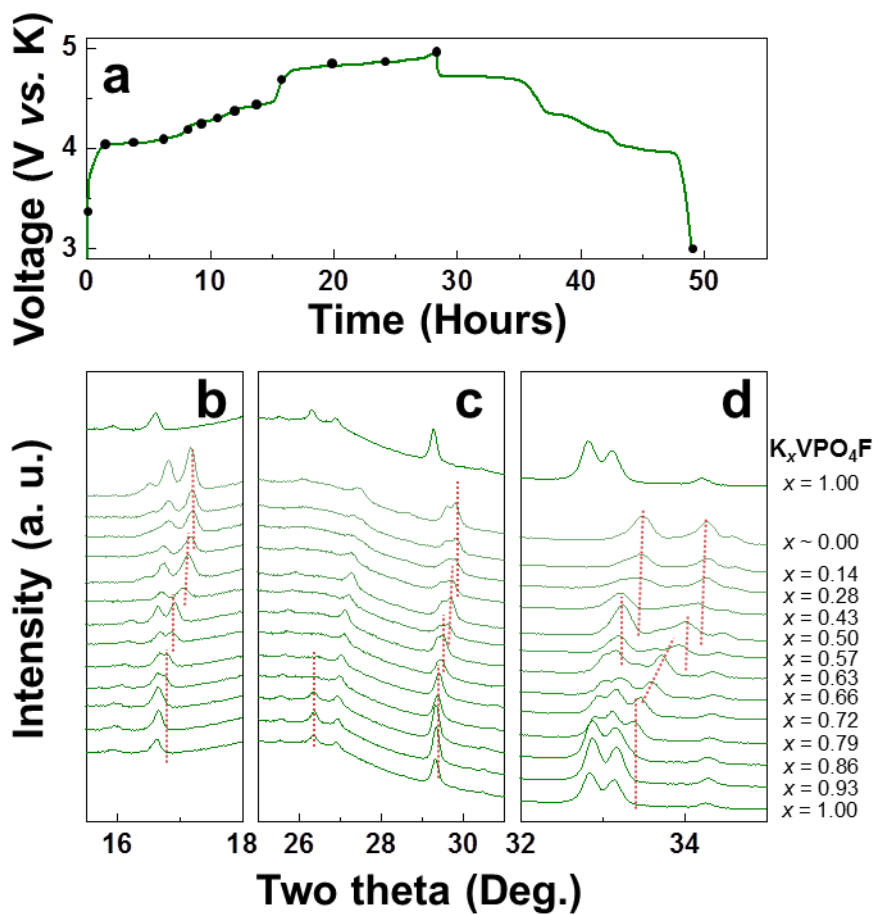
Figure 5. Structural evolution of K$_x$VPO$_4$F upon K extraction and reinsertion. a. Galvanostatic charge/discharge profile and **b–d.** XRD patterns of K$_x$VPO$_4$F samples obtained at different states of cycling.
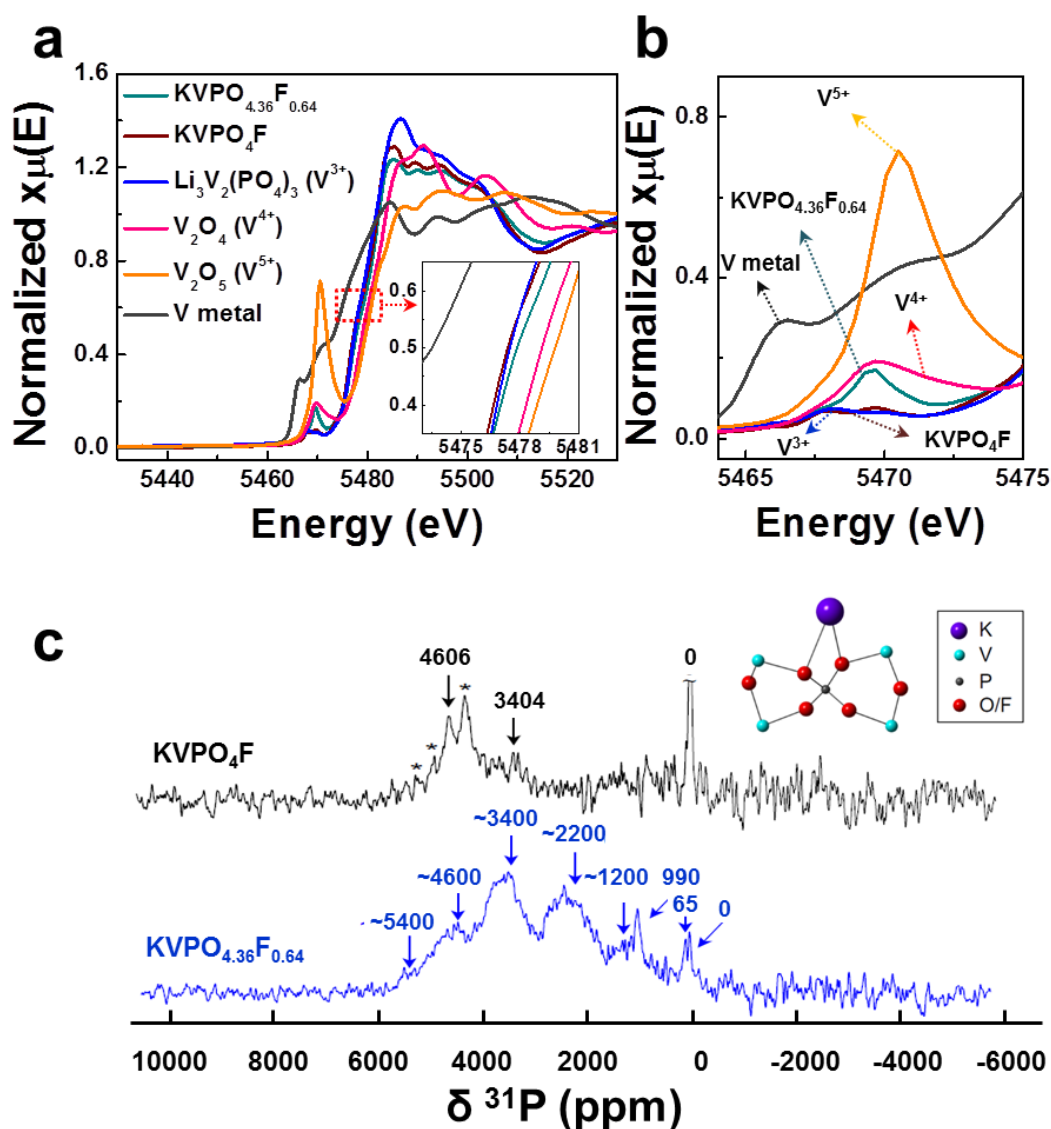
Figure 6. XANES and ^{31}P-NMR results of KVPO$_4$F and KVPO$_{4.36}$F$_{0.64}$. a. V K-edge XANES spectrum of KVPO$_4$F and KVPO$_{4.36}$F$_{0.64}$ with reference compounds of Li$_3$V$_2$(PO$_4$)$_3$, V$_2$O$_4$, V$_2$O$_5$, and V metal as references. (Inset: XANES spectrum near the inflection point of 0.5) **b.** Pre-edge region of XANES spectra **c.** ^{31}P double-adiabatic spin-echo solid-state NMR spectra collected on KVPO$_4$F and KVPO$_{4.36}$F$_{0.64}$ at 60-kHz magic angle spinning and an external field of 11.7 T. (Inset: diagram of the 31P site)

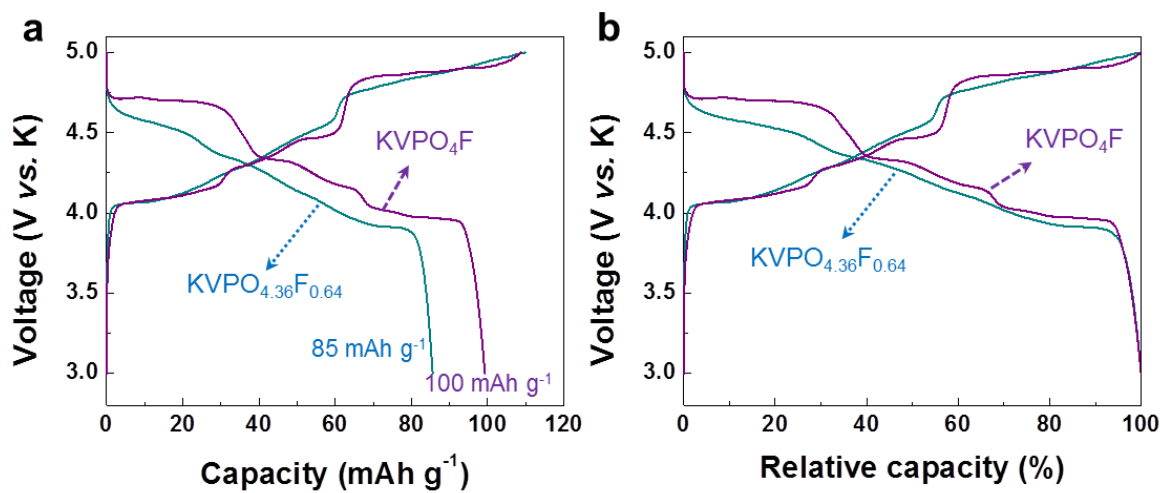**Figure 7. Galvanostatic charge/discharge profiles of KVPO₄F and KVPO₄.₃₆F₀.₆₄ in the**

2ⁿᵈ cycle. a. Capacity *vs.* voltage plot and **b.** relative capacity *vs.* voltage plot.

This work reports the stoichiometric KVPO$_4$F cathode, which delivers a reversible capacity of ~105 mAh g^{-1} with an average voltage of ~4.3 V (*vs.* K/K$^+$), resulting in a gravimetric energy density of ~450 Wh kg^{-1}. This work further investigates the structural evolution of K$_x$VPO$_4$F and oxygen substitution effect on its electrochemistry.

Keyword: K-ion battery, Cathode, Polyanion, Fluorophosphate

Haegyeom Kim, Dong-Hwa Seo, Matteo Bianchini, Raphaële J. Clément, Hyunchul Kim, Jae Chul Kim, Won-Sub Yoon, Gerbrand Ceder[*]

A new strategy for high voltage cathodes for K-ion batteries: stoichiometric KVPO$_4$F
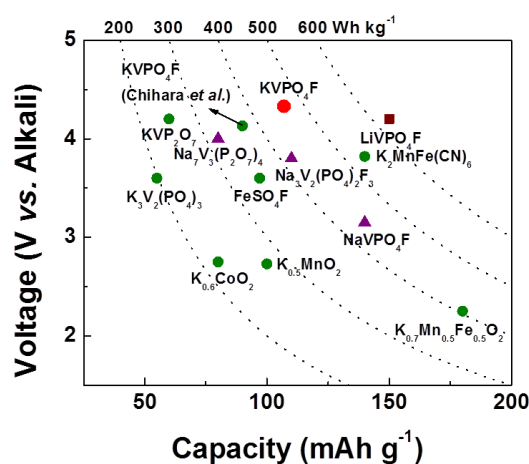
Supporting Information

A new strategy for high voltage cathodes for K-ion batteries: stoichiometric KVPO₄F

Haegyeom Kim, Dong-Hwa Seo, Matteo Bianchini, Raphaële J. Clément, Hyunchul Kim, Jae Chul Kim, Won-Sub Yoon, Gerbrand Ceder[*]

Additional details on hybrid DFT/HF calculations of paramagnetic NMR parameters

^{31}P paramagnetic NMR parameters were computed within the CRYSTAL14 all-electron linear combination of atomic orbitals (LCAO) code.[1] Two spin-polarized exchange-correlation functionals based upon the B3LYP form, with weights of Hartree-Fock (HF) exchange of 20% (B3LYP or H20) and 35 % (H35), were chosen for their satisfactory performance in determining the electronic structure, band gaps and properties of transition metal compounds (H20),[2, 3] and for their accurate determination of the magnetic coupling constants of related materials (H35)[4, 5, 6]. Moreover, previous studies on transition metal phosphates have demonstrated that the experimental NMR shift generally lies within the shift range set by the HYB20 and HYB35 computed shifts.[7, 8, 9] Two types of basis sets were employed, a smaller basis set (BS-I) was used for structural relaxations, and a larger basis set (BS-II) was used to calculate the NMR parameters, requiring an accurate description of the core electronic states. For BS-I, individual atomic basis sets were of the form (21s13p)/[1s4sp] for K, as used by Civalleri et al.[10], (20s12p4d)/[1s4sp2d] for V, (16s8p1d)/[1s3sp1d] for P, (14s6p1d)/[1s3sp1d] for O, and (10s6p1d)/[4s3p1d] for F, where the values in parentheses denote the number of Gaussian primitives and the values in square brackets the contraction scheme. All BS-I were obtained from the CRYSTAL repository and were unmodified from their previous use in a broad range of compounds.[11] For BS-II, modified IGLO-III sets were adopted for P, O and F, of the form (11s7p3d)/[7s6p3d] for P

and (10s6p2d)/[6s5p2d] for O and F,[12] a flexible and extended TZVP-derived (17s11p1d)/[6s4p1d] set was used for K, modified from [13] by increasing the exponent of the d shell, and an Ahlrichs DZP-derived (13s9p5d)/[7s5p3d] set was applied to V[14] .

Hyperfine NMR parameters were computed in the fully optimized (atomic positions and cell parameters) $KVPO_4F$ structure. All first principles structural optimizations were carried out in the ferromagnetic (FM) state, after removal of all symmetry constraints (P1 space group). Structural optimization was pursued on an 8 formula unit supercell using the quasi-Newton algorithm with RMS convergence tolerances of 10^{-7}, 0.0003, and 0.0012 au for total energy, root-mean-square (rms) force, and rms displacement, respectively. Tolerances for maximum force and displacement components were set to 1.5 times the respective rms values. Sufficient convergence in total energies and spin densities was obtained by application of integral series truncation thresholds of 10^{-7}, 10^{-7}, 10^{-7}, 10^{-7}, and 10^{-14} for Coulomb overlap and penetration, exchange overlap, and g- and n-series exchange penetration, respectively, as defined in the CRYSTAL documentation.[11] An isotropic Monkhorst-Pack[15] reciprocal space mesh with shrinking factor 4 was used for structural relaxation and paramagnetic NMR calculations of the cuboid cell (12.9 x 6.4 x 10.7 Å after relaxation). The final total energies and spin and charge distributions were obtained in the absence of any spin and eigenvalue constraints.
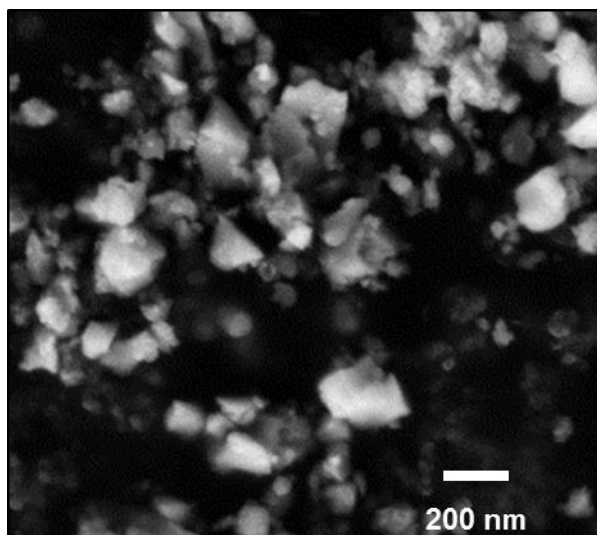
References

[1] Dovesi, R.; Orlando, R.; Erba, A.; Zicovich-Wilson, C. M.; Civalleri, B.; Casassa, S.; Maschio, L.; Ferrabone, M.; La Pierre, De, M.; D'Arco, P.; Noël, Y.; Causà, M.; Rérat, M.; Kirtman, B. *Int. J. Quantum Chem.* **2014**, *114* (19), 1287.

[2] Muscat, J.; Wander, A.; Harrison, N. M. *Chem. Phys. Lett.* **2001**, *342* (3-4), 397.

[3] Corà, F.; Alfredsson, M.; Mallia, G.; Middlemiss, D. S.; Mackrodt, W. C.; Dovesi, R.; Orlando, R. *Struct. Bonding (Berlin)* **2004**, 113, 171.

[4]Feng, X.; Harrison, N. *Phys. Rev. B* **2004**, *70* (9), 092402.

[5] Middlemiss, D. S.; Lawton, L. M.; Wilson, C. C. *J. Phys.: Condens. Matter* **2008**, *20* (33), 335231.

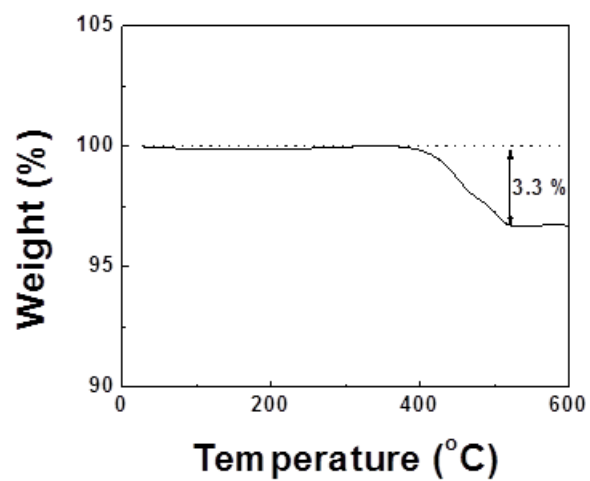[6] P R Moreira, I.; Illas, F.; Martin, R. *Phys. Rev. B* **2002**, *65* (15), 155102.

[7]Kim, J.; Middlemiss, D. S.; Chernova, N. A.; Zhu, B. Y. X.; Masquelier, C.; Grey, C. P. *J. Am. Chem. Soc.* **2010**, *132* (47), 16825.

[8] Clément, R. J.; Pell, A. J.; Middlemiss, D. S.; Strobridge, F. C.; Miller, J. K.; Whittingham, M. S.; Emsley, L.; Grey, C. P.; Pintacuda, G. *J. Am. Chem. Soc.* **2012**, *134* (41), 17178.

[9] Middlemiss, D. S.; Ilott, A. J.; Clément, R. J.; Strobridge, F. C.; Grey, C. P. *Chem. Mater.* **2013**, *25* (9), 1723.

[10] B. Civalleri, A.M. Ferrari, M. Llunell, R. Orlando, M. Merawa, P. Ugliengo, *Chem. Mater.* **2003**, *15*, 3996.

[11] Dovesi, R.; Saunders, V. R.; Roetti, C.; Orlando, R.; Zicovich-Wilson, C. M.; Pascale, F.; Civalleri, B.; Doll, K.; Harrison, N. M.; Bush, I. J.; D'Arco, P.; Llunell, M.; Causà, M.; Noël, Y. *CRYSTAL14 User's Manual*; University of Torino: Torino, Italy, 2014.

[12] Kutzelnigg, W.; Fleischer, U.; Schindler, M. In *Deuterium and Shift Calculation*; Springer, Berlin, Heidelberg, **1990**, 165.

[13] M. F. Peintinger, D. V. Oliveira, and T. Bredow, *J. Comput. Chem.*, **2013**, 34, 451–459 (2013).

[14] Schäfer, A.; Horn, H.; Ahlrichs, R. *J. Chem. Phys.* **1992**, 97, 2571.

[15] Monkhorst, H. J.; Pack, J. D. *Phys. Rev. B* **1976**, *13* (12), 5188.

Supplementary Table 1. Structural parameters for $KVPO_4F$ obtained from Rietveld refinement of synchrotron XRD data. z/c of V1 was fixed due the floating origin along c of the Pna21 space group.

atom	Wyckoff position	Atomic position			Occ.	B_{iso}
		x/a	y/b	z/c		
V1	4a	0.3846(2)	0.4968(7)	0.0052(-)	1	0.75(5)
V2	4a	0.2478(4)	0.2497(7)	0.254(1)	1	0.54(4)
P1	4a	0.5008(7)	0.3295(6)	0.257(1)	1	0.77(5)
P2	4a	0.1809(3)	0.499(1)	0.504(1)	1	0.77(5)
K1	4a	0.388(1)	0.798(2)	0.312(2)	0.5	1.8(1)
K1'	4a	0.374(1)	0.759(2)	0.309(2)	0.5	1.8(1)
K2	4a	0.108(2)	0.709(2)	0.051(2)	0.5	1.8(1)
K2'	4a	0.103(2)	0.690(3)	0.079(2)	0.5	1.8(1)
O1	4a	0.1809(3)	0.499(1)	0.504(1)	1	0.44(6)
O2	4a	0.387(1)	0.798(2)	0.312(2)	1	0.44(6)
O3	4a	0.374(1)	0.759(2)	0.309(2)	1	0.44(6)
O4	4a	0.108(2)	0.709(2)	0.051(2)	1	0.44(6)
O5	4a	0.103(2)	0.690(2)	0.079(2)	1	0.44(6)
O6	4a	0.484(1)	0.488(2)	0.147(1)	1	0.44(6)
O7	4a	0.509(2)	0.470(2)	0.376(1)	1	0.44(6)
O8	4a	0.399(1)	0.199(2)	0.283(2)	1	0.44(6)
F1	4a	0.270(1)	0.473(2)	0.129(1)	1	1.0(1)
F2	4a	0.231(1)	0.020(3)	0.380(1)	1	1.0(1)

Table header block:

KVPO₄F

Space group: Pna2₁; Z = 8
a = 12.8423(1) Å, b = 6.40785(3) Å, c = 10.62974(6) Å
V = 874.74(1) Å³, V/Z = 109.34(1) Å³ χ^2 = 3.27, R_{bragg} = 4.61 %, R_{wp} = 12.2%
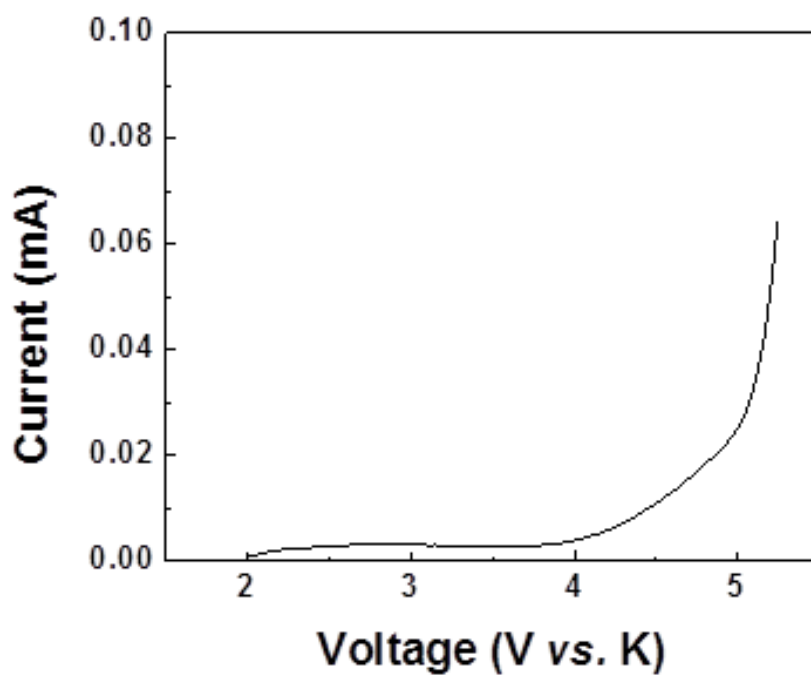
**Supplementary Figure 1.** Scanning electron microscopy image of KVPO$_4$F.

**Supplementary Figure 2.** TGA analysis of KVPO$_4$F.
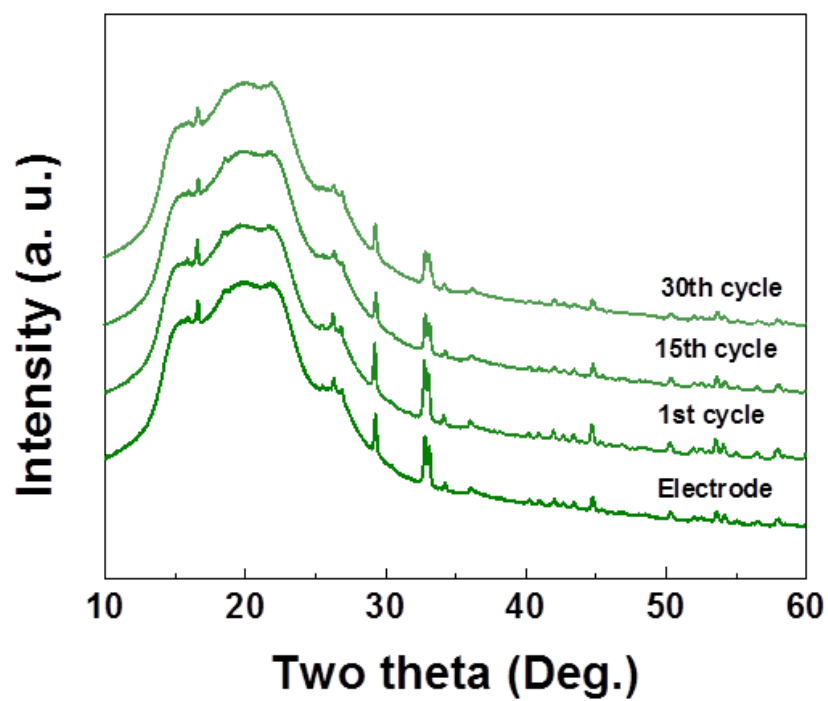
Supplementary Figure 3. *Ex situ* XRD patterns of KVPO$_4$F after the 1st, 15th and 30th cycle.

Supplementary Figure 4. Linear scan voltage measurement of the electrolyte. 0.7 M

KPF_6 in EC/DEC is used as the electrolyte and K metal is used as the counter electrode.
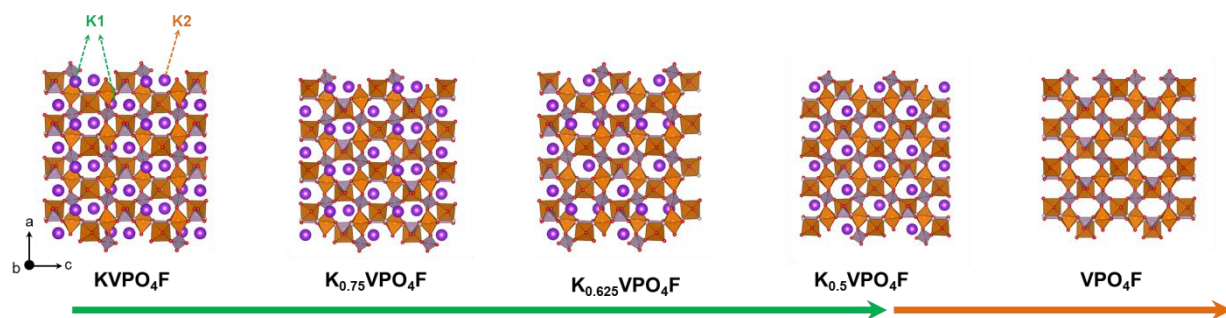
Supplementary Figure 5. Simulated crystal structure of K_xVPO_4F when x = 1.0, 0.75, 0.625, 0.5, and 0.0, as obtained from DFT calculations.
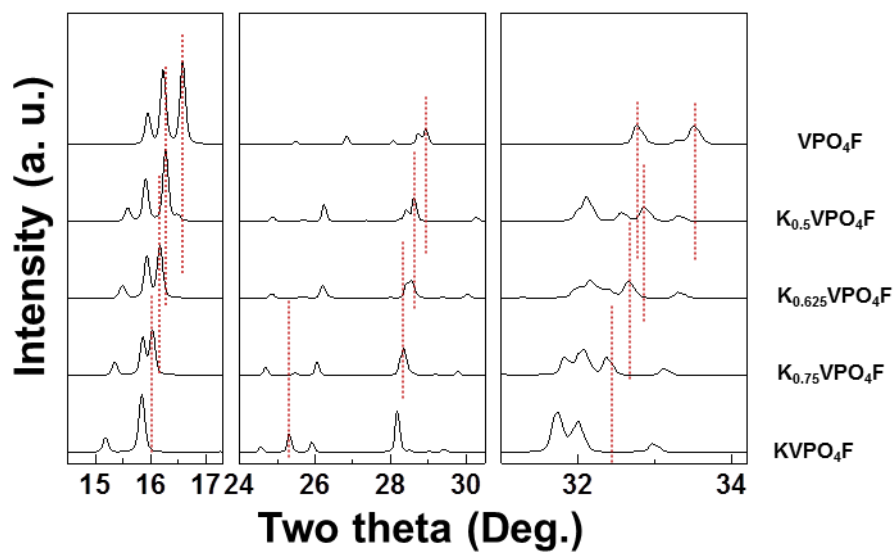
Supplementary Figure 6. Simulated XRD patterns of K_xVPO_4F when $x = 1.0, 0.75, 0.625,$

0.5, and 0.0 based on the crystal structures obtained from DFT calculations.

Supplementary Table 2. Refined lattice parameters of $K_x VPO_4 F$ (x = 1.0, 0.75, 0.625, 0.5, and 0.0) of *ex situ* XRD using structures obtained from DFT calculations.

|	a (Å)	b (Å)	c (Å)	V (Å³)
KVPO$_4$F	12.8425	6.4078	10.6298	874.76
K$_{0.75}$VPO$_4$F	12.8180	6.3402	10.5967	861.19
K$_{0.625}$VPO$_4$F	12.8028	6.2977	10.5885	853.73
K$_{0.5}$VPO$_4$F	12.8113	6.2154	10.5842	842.80
VPO$_4$F	12.6567	6.1413	10.5185	817.56
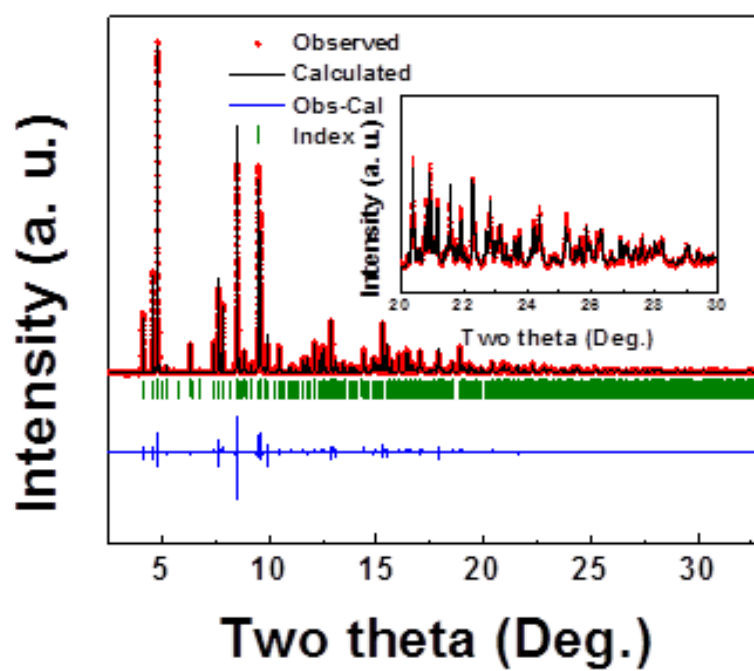
Supplementary Figure 7. Synchrotron-based X-ray diffraction analysis of $KVPO_{4.36}F_{0.64}$ (wavelength = 0.457 Å). (Inset: Enlarged X-ray diffraction pattern from 20º to 30º.)

Supplementary Table 3. Structural parameters for $KVPO_{4.36}F_{0.64}$ structure obtained from Rietveld refinement of synchrotron XRD data. The relative O and F occupancies were not refined due their light weight and the impossibility to distinguish them with X-Rays. z/c of V1 was fixed due the floating origin along c of the Pna21 space group.

$KVPO_{4.36}F_{0.64}$					
Space group: Pna2$_1$; Z = 8					
a = 12.8235(1) Å, b = 6.39630(6) Å, c = 10.5860(1) Å					
V = 868.30(1) Å^3, V/Z = 108.54(1) Å^3			χ^2 = 10.9, R_{bragg} = 5.39 %, R_{wp} = 20.5%		

atom	Wyckoff position	Atomic position			Occ.	B_{iso}
		x/a	y/b	z/c		
V1	4a	0.3820(3)	0.498(1)	0.0049(-)	1	0.54(8)
V2	4a	0.2470(6)	0.256(1)	0.255(1)	1	0.77(8)
P1	4a	0.499(1)	0.3319(9)	0.262(1)	1	0.59(8)
P2	4a	0.1821(5)	0.498(2)	0.508(1)	1	0.59(8)
K1	4a	0.390(2)	0.788(3)	0.327(3)	0.5	1.3(1)
K1'	4a	0.375(2)	0.773(4)	0.303(2)	0.5	1.3(1)
K2	4a	0.105(2)	0.701(3)	0.049(2)	0.5	1.3(1)
K2'	4a	0.105(2)	0.702(3)	0.088(2)	0.5	1.3(1)
O1	4a	0.482(2)	0.484(3)	0.149(2)	1	0.23(1)
O2	4a	0.508(2)	0.467(3)	0.385(2)	1	0.23(1)
O3	4a	0.401(2)	0.199(3)	0.286(2)	1	0.23(1)
O4	4a	0.597(2)	0.189(3)	0.240(2)	1	0.23(1)
O5	4a	0.108(2)	0.313(3)	0.539(3)	1	0.23(1)
O6	4a	0.112(2)	0.692(4)	0.479(2)	1	0.23(1)
O7	4a	0.251(2)	0.532(4)	0.627(2)	1	0.23(1)
O8	4a	0.254(2)	0.457(4)	0.399(3)	1	0.23(1)
F1	4a	0.275(2)	0.477(4)	0.138(2)	1	1.4(2)
F2	4a	0.227(2)	0.038(5)	0.390(2)	1	1.4(2)

Supplementary Table 4. First principles ^{31}P Fermi contact NMR shifts (δ_{FC}) for the two P sites present in $KVPO_4F$. The difference ($\Delta\delta_{FC}$) between the shifts of P1 and P2 is reported for comparison with the shift difference between the two signals observed in the ^{31}P NMR spectrum. δ_{FC} values were derived from the spin density at the ^{31}P nucleus obtained from hybrid DFT/HF calculations using the HYB20 and HYB35 functionals (containing 20 and 35% Hartree-Fock exchange, respectively). The spin density was scaled by a magnetic scaling factor $\Phi = 0.0262$ further discussed in the methods section. δ_{FC} values reported in this table are averages over all P1 and P2 sites in the cell.
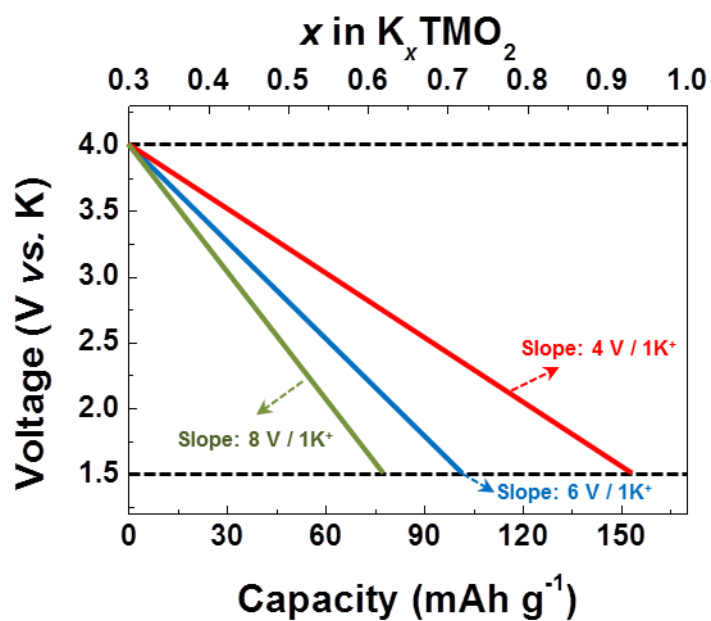
	HYB20	HYB35
$\delta_{FC}(P_1)$ / ppm	6688	5425
$\delta_{FC}(P_2)$ / ppm	5217	4238
$\Delta\delta_{FC} = \delta_{FC}(P_1) - \delta_{FC}(P_2)$ / ppm	1471	1187
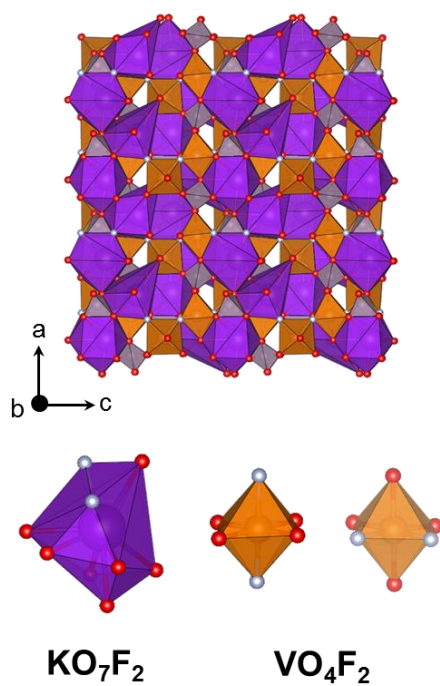
Supplementary Figure 8. Local K and V environments in KVPO$_4$F.
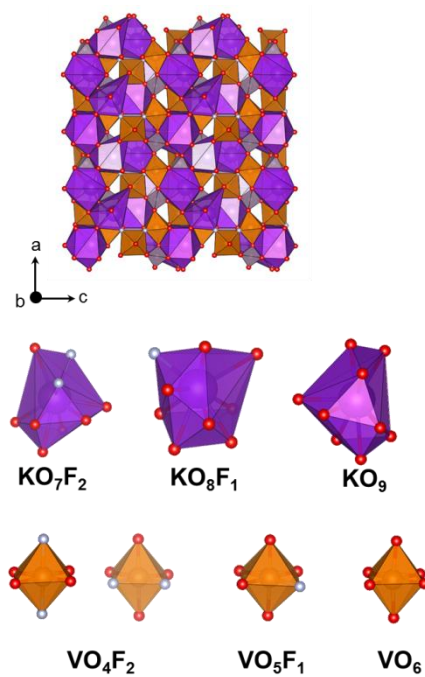
Supplementary Figure 9. Local K and V environments in KVPO$_{4.375}$F$_{0.625}$.

Supplementary Figure 10. Schematic voltage curves of K-TMO$_2$ cathodes with different voltage slopes.